Quantifying spatial and temporal scales of phytoplankton variability in the Sub-Antarctic Ocean using a high-resolution glider dataset

Hazel Jean Little

A thesis presented for the degree of Masters of Science

Department of Oceanography

University of Cape Town

Plagiarism Declaration

I know the meaning of plagiarism and declare that all of the work in the dissertation (or thesis), save for that which is properly acknowledged, is my own.

Hazel Little

15 August 2016

Supervisors

Dr. Sandy Thomalla

Southern Ocean Carbon and Climate Observatory, CSIR, Rosebank, South Africa

Dr. Sebastiaan Swart

Southern Ocean Carbon and Climate Observatory, CSIR, Rosebank, South Africa

Associate Professor Marcello Vichi

Department of Oceanography, University of Cape Town, Rondebosch, Cape Town, South Africa

Abstract

Phytoplankton in the Sub-Antarctic Southern Ocean have a distinct seasonal cycle, which is highly variable in both space and time. The seasonal and spatial distribution of chlorophyll can be attributed to the complex nature of the physical and biogeochemical factors controlling phytoplankton production.

Studies show that high-resolution sampling is required to understand variability in phytoplankton distribution and primary production. In this study, high-resolution glider data sampled in the Atlantic Sub-Antarctic Zone are used to characterise the scales of phytoplankton variability. Continuous glider data provide a novel way to assess phytoplankton variability at small time and space scales (meso- to submesoscale), especially in an area that has a lack of continuous measurements, which are necessary for addressing climate related questions. Temporal variability of phytoplankton was investigated using Empirical Mode Decomposition of surface chlorophyll-a concentrations collected from a Seaglider over a period of 5.5 months (25 September 2012 to 15 February 2013). This study found that during spring, chlorophyll-a concentrations were dominated by small scale daily fluctuations as well as by the rising seasonal ramp due to seasonal stratification. The removal of these signals revealed that the chlorophyll-a variability was dominated by submesoscales. In spring, phytoplankton blooms occurred as a result of features that shoaled the mixed layer depth when the wind stress weakened, elevating light conditions for short periods and allowing increased growth. In summer phytoplankton blooms were found to occur at submesoscales periods as well. This variability was found to be driven by synoptic storms varying the strength of the wind stress and consequently the mixed layer depth (that alters the nutrient and light environment). Additionally, through reconstructing the time series through subsampling at the dominant signals, this study found that in order to accurately resolve and characterise the multi-seasonal variability of phytoplankton, chlorophyll needs to be sampled at high frequencies (<10 days). Spatial variability was investigated using daily MODIS ocean colour and sea surface temperature images coincident with the glider track. Spatial variability was characterised by the variance calculated at different length scales. Spatial analysis found that phytoplankton were patchier in both spring and summer when compared to sea surface temperature, at all length scales and that a greater variance was contained at small scales. There was also a greater variance in summer chlorophyll-a compared to spring due to higher maximum biomass. Further spatial analysis compared satellite spatial variance with glider measurements at the same length scale (70 km). This study found that a third of the variability found by the glider was caused by spatial patchiness, while the remainder could be contributed by local growth.

These dominant meso- and submesoscale changes in chlorophyll-a at both temporal and spatial scales, highlights the need to resolve for both meso- to submesoscales in order to accurately reflect phytoplankton seasonal variability and ultimately to understand the impact of phytoplankton variability on carbon flux.

Acknowledgements

I have been fortunate enough to have three supervisors involved in my MSc, each contributing in different ways to get me to this point. Dr Seb Swart and Dr Sandy Thomalla first took me on in my honours and then my masters, while Dr Marcello Vichi enthusiastically joined in for my masters.

To Dr Seb Swart, without whom the glider project in South Africa would not exist, nor would part my master's thesis. Thank you Seb for your enthusiasm for the gliders and for always helping me attempt to understand the physics behind phytoplankton variability.

To Dr Sandy Thomalla, your expertise in Southern Ocean biogeochemistry and willingness to explain how phytoplankton work has truly been appreciated. Thank you for always being willing to simplify things for me when they get to mathematical. Sandy, you have also allowed me the opportunity to work at sea, were I was able to gain practical experience in collecting and analysing data. These opportunities have allowed me to learn more about the importance of my project as well as getting involved in a successful ocean science program. Thank you.

To Associate Professor Marcello Vichi, thank you for helping me with all the statistics in my project and explaining why we need them. Thank you for re-looking at your Master's script and helping me add even more loops to it. Finally, thank you for filling out a lot of admin forms and for your patience in answering questions or re-explaining things to me.

Thank you to Dr Raymond Roman and Christo Whittle for assisting me in the rendering of raw satellite data and the use of SeaDAS (it took a long time to install). Marcel du Plessis for helping me get started with EMD analysis and for the wind stress and mixed layer depth data. Derek Needham, Andre Hoek, JP Smit and Sinekhaya Bilana from Sea Technology Services, who run the glider operations for SOSCEx. To my fellow master's students and friends: Khushboo, Marc, Mhlanga, Ramontsheng, Tharone, Tania, Clara, Jess and Roger, thank you for all the laughs, breaks, cups of tea and help over the last two years.

To my family, thank you for all the love and support you have given my over the last two years and throughout my life. Thank you for all the interest in my work over the years, especially with this project. Thank you for all the opportunities you have provided me with over the years. I have truly appreciated it and learnt a lot from all of you.

To my best friend, Graeme, thank you for your endless patience and encouragement over this period. For understanding when I needed to work or needed a break. For celebrating achievements big or small, and for listening to me talk about my project when it was gibberish to you and still being enthusiastic about it. I am very grateful for everything. Thank you!

Funding

I would like to thank CSIR and National Research Foundation of the Department of Science and Technology, South Africa for financial support through the award of the CSIR/NRF Grant for the tenure of my Master of Science degree.

Acronyms

AAZ:	Antarctic Zone
ACC:	Antarctic Circumpolar Current
APF:	Antarctic Polar Front
Bb:	Optical Backscattering
Chl-a:	Chlorophyll-a
Chloro_a:	Chlorophyll-a
CO_2:	Carbon Dioxide
EMD:	Empirical Mode Decomposition
IMF:	Intrinsic Mode Functions
MLD:	Mixed Layer Depth
MODIS:	Moderate-resolution Imaging Spectroradiometer
NPQ:	Non-photochemical quenching
PAR:	Photosynthetically Active Radiation
POC:	Particular Organic Carbon
RMSE:	Root mean square error
sACCf:	Southern Antarctic Circumpolar Current Front
SAF:	Subantarctic Front
SAZ:	Subantarctic Zone
SBdy:	Southern Boundary
SG573:	Seaglider 573
STF:	Subtropical Front
SST:	Sea Surface Temperature

Table of Contents

List of Figures

List of Tables

Chapter 1:

Literature Review

1.1 Southern Ocean

The Southern Ocean covers 22% of the total ocean surface and plays a major role in the global climate system. It is the only ocean in the world with no zonal boundary (Olbers et al., 2004). The Southern Ocean interconnects three other major ocean basins allowing it to transmit climate signals from one region to another (Gille, 2002). The largest current in the world, the Antarctic Circumpolar Current (ACC) is found in the core of the Southern Ocean (~45-55˚S). As the ACC flows eastward, driven by an intense band of westerly winds, it absorbs and mixes heat and salt from the Atlantic, Indian and Pacific Oceans and redistributes these properties northwards into the Atlantic Ocean (Cunningham et al., 2003). This redistribution of heat and salt is vital in the global meridional overturning circulation, making the Southern Ocean a major contributor to the coupling of the global ocean-atmosphere climate system.

The Southern Ocean is characterised by distinguishable temperature gradients in water mass properties, from warm subtropical waters in the north to cold polar waters in the south. Temperature gradients, together with north-south density gradients, characterise the Southern Ocean into zones with frontal bands (Orsi et al., 1995; Belkin and Gordon, 1996). The Sub-Antarctic Zone (SAZ) represents more than half of the areal extent of the Southern Ocean (Orsi et al., 1995) and plays an important role in the ocean-atmosphere climatic system. The SAZ is defined by the Subtropical Front (STF), the northern boundary of the Southern Ocean which separates warmer, saltier subtropical waters to the north from cooler, fresher subantarctic waters in the SAZ. The Subantarctic Front (SAF), the northern most boundary of the ACC neighbours the STF to the south and marks the start of the cold Antarctic waters (Orsi et al., 1995). The Southern Ocean also has the Antarctic Polar Front (APF), which combined with the SAF, is considered to be the core of the ACC, while the southern ACC front (sACCf) and the Southern Boundary (Sbdy) of the ACC are encompassed in the Antarctic Zone (AAZ), south of the SAF (Figure 1.1). These fronts are characterised by intense mesoscale (10-100 km) modes of variability, where filaments are created by meanders of fronts, eddies and intense lateral gradients in temperature (Sokolov and Rintoul, 2007; Arhan et al., 2011). As a result, they are the dominant physical control on biochemical distributions in the Southern Ocean (Deacon, 1933) and are thus a critical part of the global ocean circulation and biogeochemical cycles of nutrients and carbon (Arrigo et al., 2008).

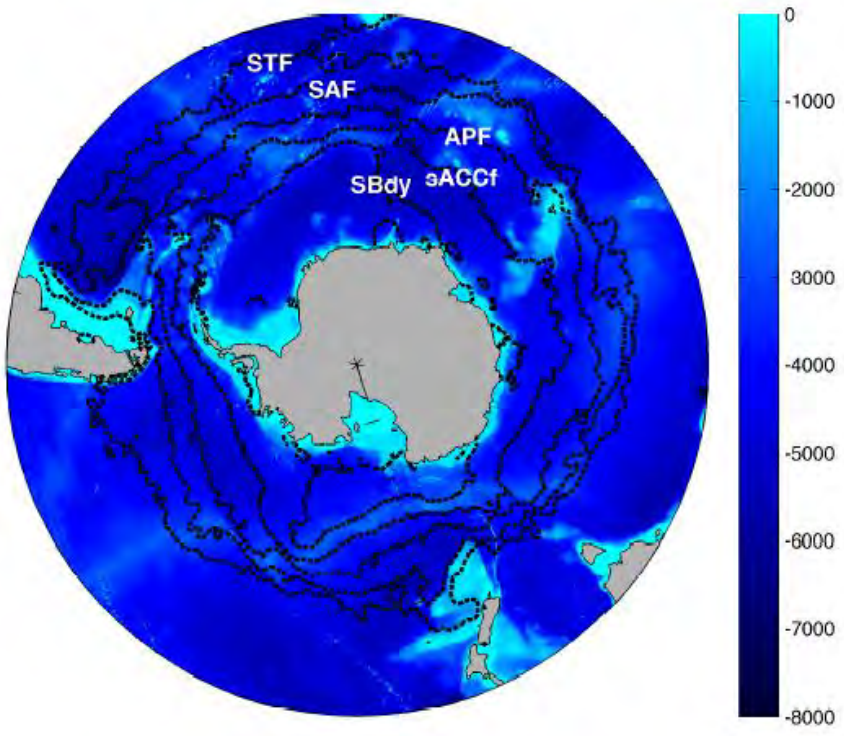

Figure 1.1 The mean position of the circumpolar frontal bands (dotted black lines) in the Southern Ocean determined from satellite altimetry (Swart and Speich, 2010) over the period (25 September 2012 to 15 February 2013) of the Southern Ocean Seasonal Cycle Experiment (SOSCEx). Form north to south, the Subtropical Front (STF), Subantarctic Front (SAF), Antarctic Polar Front (APF), southern Antarctic Circumpolar Current front (sACCf) and the Southern Boundary (SBdy). Ocean bathymetry is acquired from the ETOPO1 dataset (meters below sea level). Figure from du Plessis 2014.

1.2 Biogeochemistry of the Southern Ocean

Global atmospheric carbon dioxide (CO_2) levels have risen dramatically over the last century from increased usage of fossil fuels as the primary source of power in industrial processes and modernisation. The ocean is the primary sink for anthropogenic CO_2, having absorbed an estimated ~48±9% of the global anthropogenic CO_2 emitted over the last industrial period (1880-1994) (Mikaloff Fletcher et al., 2006). Of the world's oceans, the Southern Ocean has contributed to the greatest amount of anthropogenic CO_2 uptake, with ~23% of the global total anthropogenic CO_2 ocean uptake occurring between 44˚S - 58˚S (Mikaloff Fletcher et al., 2006; Takahashi et al., 2012). As such, the Southern Ocean in particular is slowing the rate of atmospheric CO_2 increase and the effects of human-driven climate change. Monitoring and understanding spatial and temporal changes in air-sea CO_2 flux in the Southern Ocean is thus critical for an improved understanding of the global carbon cycle and the prediction of future atmospheric CO_2 conditions.

The Southern Ocean accounts for the removal of approximately 3 Pg C annually from the atmosphere south of 30˚S (Schlitzer, 2002). This oceanic CO_2 uptake occurs through two mechanisms, the solubility and biological carbon pumps (Figure 1.2). The solubility pump is the physical-chemical processes that transports carbon from the atmosphere into the ocean as dissolved inorganic carbon. The solubility pump is dependent on the temperature and thermal stratification of the ocean (Ito and Follows, 2003), where colder waters are enriched in more dissolved inorganic carbon due to their higher solubility. The biological pump is the mechanism by which organic carbon is sequestered into the deep ocean by phytoplankton, when CO_2 is fixed into particulate organic carbon during photosynthesis. When the phytoplankton sink, or are otherwise transported to the deep ocean, a CO_2 pressure gradient is created in surface waters between the ocean and atmosphere that allows more CO_2 to absorb into the ocean (Arrigo et al., 2008). Understanding the conditions for phytoplankton growth and development in the Southern Ocean is therefore crucial for accurate predictions of the biological carbon pump and improved long term trajectories of the global carbon cycle. In spite of this, a complete understanding of the phytoplankton temporal and spatial distribution and associated physical, ecological and physiological drivers in the Southern Ocean is lacking (Thomalla et al., 2011).

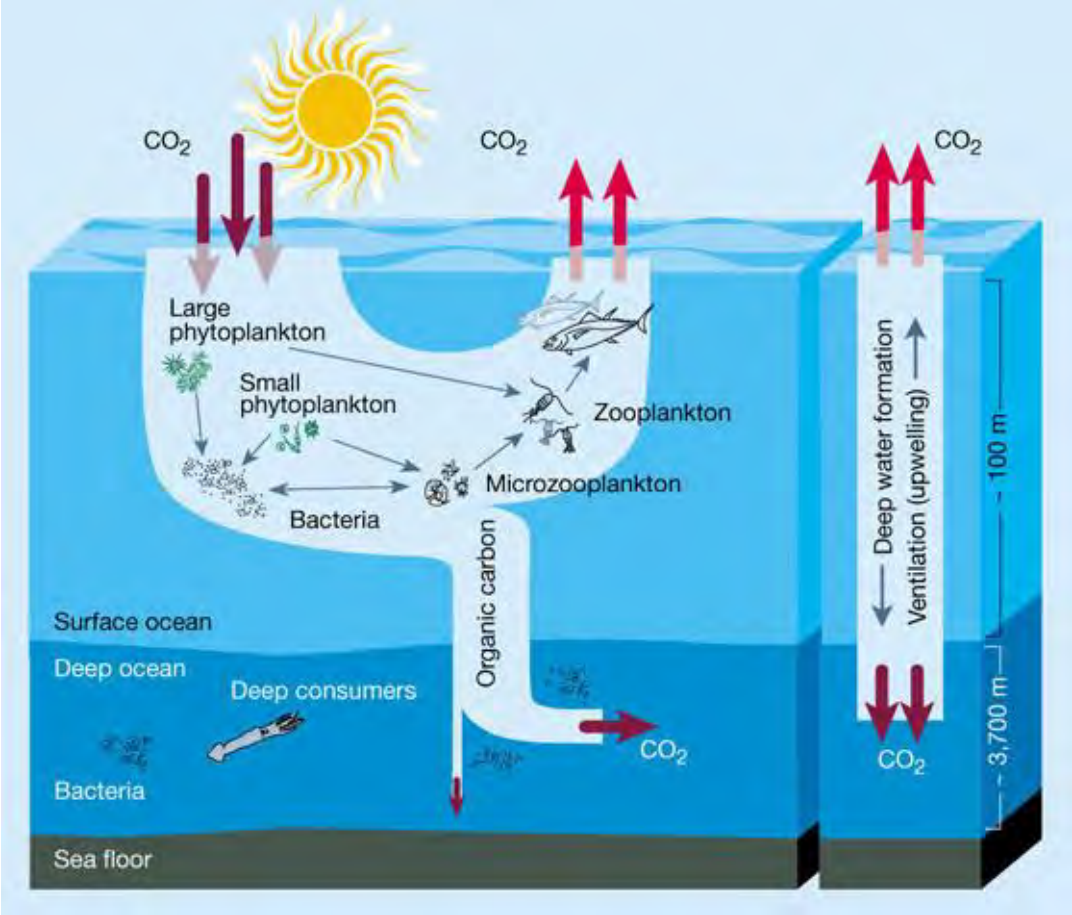

Figure 1.2 Carbon uptake and release into and out of the ocean through the biological (left) and solubility (right) pumps. Figure taken from Chisholm 2000.

1.3 Phytoplankton in the Southern Ocean and scales of variability

Although the Southern Ocean has the greatest inventory of unused macro-nutrients in the world ocean (Levitus et al., 1993), it has relatively low phytoplankton concentrations. These low concentrations of phytoplankton (relative to the macro nutrient supply), predominantly in the pelagic waters, are due to a number of factors that include bottom up controls of light, iron and silicate limitations as well as top down controls of grazing by zooplankton (Arrigo et al., 1998; Boyd, 2002a). Intense phytoplankton blooms can develop in areas, for example where iron limitation is relieved (Boyd et al., 2000; Blain et al., 2007; Pollard et al., 2009), however these tend to be highly variable, both spatially and temporally (Arrigo et al., 2008).

1.3.1 Seasonal cycle

Chlorophyll (chl-a) is the primary photosynthetic pigment of phytoplankton and can be used as a biomass proxy. In the Southern Ocean the seasonal cycle of phytoplankton biomass is typically characterised by having low chl-a concentrations in winter and high, yet spatially variable concentrations in summer (Boyd et al. 2011). The strong seasonal cycle has been attributed to the seasonal cycle of solar radiation and its impact on the vertical stability of the water column through heat flux (Sverdrup, 1953; Boyd et al., 1999; Boyd, 2002; Arrigo et al., 2008). Cooler temperatures in winter drive convective overturning that results in deep mixed layers, low light conditions and decreased rates of production with subsequent low biomass in winter. Increased heating in summer drives stratification, shallower mixed layers and improved light conditions for increased production and biomass accumulation. However, observations of surface chl-a from satellite data show that phytoplankton blooms do not follow one dominant seasonal cycle (Moore and Abbott, 2002; Thomalla et al., 2011; Carranza & Gille, 2014; Salle et al., 2015). From an analysis of 9 years of satellite surface chl-a data, Thomalla et al. (2011) found large regions in the Southern Ocean where chl-a can be characterised as having high intra-annual and intra-seasonal variability (i.e., low seasonal cycle reproducibility), while other regions were characterised as having high seasonal cycle reproducibility (i.e. a predictable seasonal cycle where every year looked like the climatological mean) (Figure 1.3). Thomalla et al. (2011) went on further to explore the sub-seasonal characteristics of the seasonal cycle and proposed that the variety of spatial and seasonal distributions were a result of the complex sub-seasonal interplay between light and nutrients (iron), which together control phytoplankton growth in the Southern Ocean. They concluded that an understanding of the seasonal, sub-seasonal and meso- to submesoscale regional characteristics of bloom dynamics and their associated physical drivers was necessary to understand the sensitivity of the response of ocean productivity to climate change.

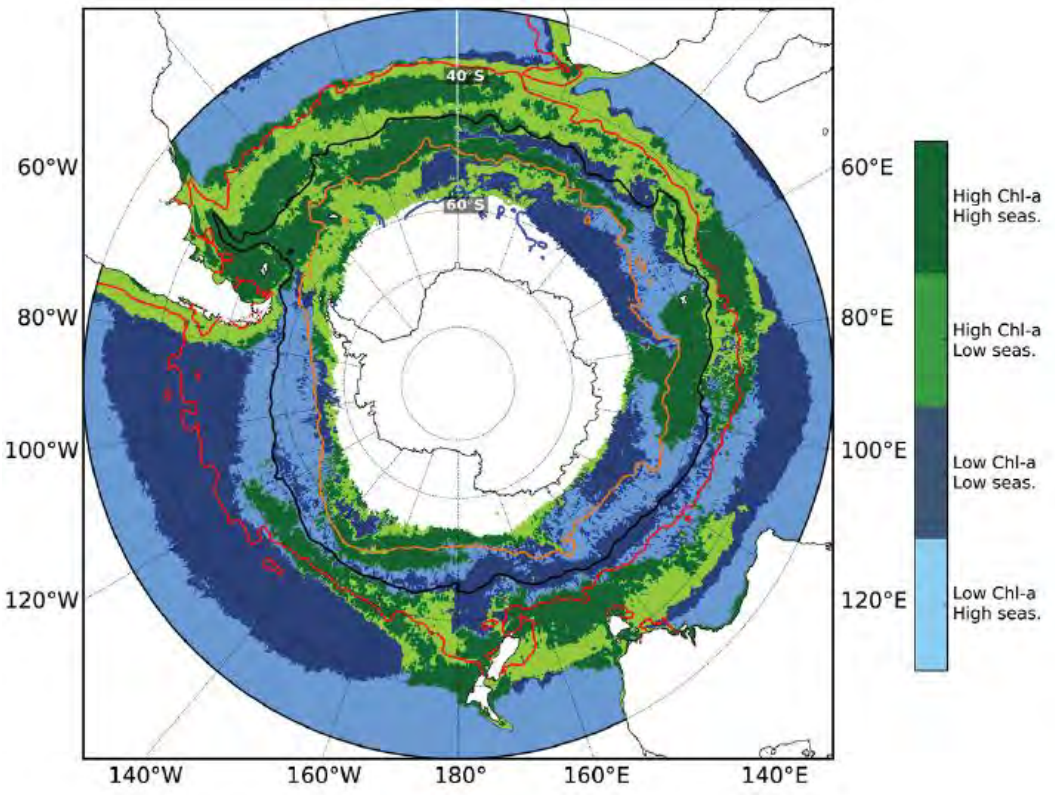

Figure 1.3 A composite of the seasonal cycle reproducibility of summer chl-a in the Southern Ocean from Thomalla et al. (2011). Regions in blue represent regions of low (<0.25 mg m^{-3}) chl-a concentrations with either high seasonal cycle reproducibility (R^2 > 0.4) (Region A, light blue) or low seasonal cycle reproducibility (R^2 < 0.4) (Region B, dark blue). Regions in green represent regions of high chl-a concentrations (> 0.25 mg m^{-3}) with either high seasonal cycle reproducibility (Region C, dark green) or low seasonal cycle reproducibility (Region D, light green). Mean (1998-2007) frontal positions are shown for the STF (red), the SAF (black), the PF (yellow) and the SACCF (pink).

1.3.2 Scales of variability

Given the critical role of small scale (seasonal to sub-seasonal and meso- to submesoscales) processes in driving the characteristics of phytoplankton distribution (particularly in the Southern Ocean), it is important that we understand how these processes work. Below is a summary from a number of *in situ* and model studies from various ocean regions that investigates how and to what extent meso- and submesoscale processes drives phytoplankton variability.

1.3.2.1 Meso- and submesoscales of variability

Numerous studies that investigated mesoscale (10 – 100km) variability of surface chl-a have found that fronts and mesoscale eddies are a major driver of phytoplankton patchiness, through the injections of

nutrients into the euphotic zone (layer of surface water that receives a sufficient amount of light for photosynthesis to occur) (McGillicuddy et al., 1998; Mahadevan and Archer, 2000; Levy et al., 2001). Using an ecosystem model embedded in a physical model, Spall and Richard (2000) investigate the impact of mesoscale frontal instabilities on the generation of phytoplankton patchiness in an open ocean frontal region. The model showed that instabilities in a mesoscale front introduced patchiness into phytoplankton communities at a variety of length scales. In addition, increases in primary production were observed locally by an order of 100% and when averaged over the frontal region by an order of 10%. Mahadevan and Archer (2000) investigated a range of model resolutions at mesoscales (40 km to 10 km) in a coupled physical-biogeochemical model. Their results showed that primary production increased (up to a factor of three) when model resolution was increased from 40 to 10 km to include mesoscale features. As such, these mesoscale instabilities and eddies (of an order of 10–100 km) have a significant impact on phytoplankton variability and on the ocean's primary productivity (McGillicuddy, 2016).

Numerical studies in recent years (Spall and Richards, 2000; Levy et al., 2001) have identified that mesoscale dynamics are responsible for an increase in numerical estimates of primary production by up to 30%. However, in most of these studies, the numerical resolution resolved mesoscale dynamics well, but poorly resolved sub-mesoscales. Other studies (Mahadevan and Archer, 2000; Levy et al., 2001) have since suggested that submesoscale physics could also significantly impact primary production. A numerical study in an oligotrophic regime by Levy et al. (2001) found that submesoscale physics was responsible for more than a third of large scale primary production. Similarly, through high-resolution satellite imagery, researchers have recognised that not resolving for submesoscale features (1-10km) can result in errors of up to 50% in primary production estimates (Levy et al., 2001; Glover et al., 2008). This shows that high spatial and temporal resolution is required to understand submesoscale phytoplankton variability in order to accurately estimate primary production, from observations or numerically.

Submesoscale physical processes have been found to be particularly relevant to understanding the variability in phytoplankton distribution due to the similarity between the timescales of submesoscale physical variability and phytoplankton growth. The variability occurs at spatial scales of an order of 0.1–10 km and on timescales of a few inertial periods (∼days) (Levy et al., 2014; Mahadevan, 2016). Submesoscale physics contributes to phytoplankton variability in various ways, depending on local environmental conditions (nutrient distribution, light environment and dynamics) and the growth of

phytoplankton species themselves (Mahadevan, 2016). Spatiotemporal distributions of phytoplankton are a result of both vertical and horizontal submesoscale processes (Martin et al., 2002; Martin, 2003; Pasquero et al., 2005) injecting nutrients into the euphotic zone or moving phytoplankton towards or away from the light (Mahadevan, 2016). These dynamical processes occur in subtropical and subpolar gyres, the Artic and Southern Oceans, continental shelves and coastal seas and are the result of fronts, mixed layer instabilities, surface forcing by the wind on eddies, nonlinear interactions from Ekman pumping and symmetric instabilities (Mahadevan, 2016).

In nutrient-depleted regions such as the subtropical gyres, Ekman pumping acts in a downward direction and diapyncal mixing is weak, however phytoplankton blooms still form. This is because of submesoscale dynamics that enhance the vertical transport of nutrients from the subsurface into the euphotic zone (Levy et al., 2001; Klein and Lapeyre, 2009; Mahadevan, 2016). This advection of nutrients tends to occur along the isopyncal surfaces when the isopyncals are sloping upward (Mahadevan, 2016). The enrichment of nutrients into the euphotic zone increases phytoplankton productivity and leads to small scale phytoplankton variability, similar to what is attained through mesoscale dynamics but in smaller areas and more episodically (Levy et al., 2001; Mahadevan, 2016).

Many of the most productive regions in the world's ocean are regions that are light limited (e.g. the Southern Ocean) and have an abundance of nutrients in the upper ocean. These regions experience large seasonal variations in mixed layer depth, with a deep mixed layer in winter and a shallower mixed layer in summer. During spring, when the wind stress weakens, the strength of mixing in the mixed layer weakens as well. A weakening of the mixing enables submesoscale eddies to stratify the mixed layer through a slumping of the isopycnals at local fronts (Mahadevan et al., 2012). The submesoscale restratification is very heterogeneous in space and thus creates highly variable mixed layer depths that exposes the phytoplankton to varying degrees of light. Phytoplankton in the upper stratified regions experience rapid growth and patchy phytoplankton blooms (Mahadevan et al., 2012). Thus, in light limited regions phytoplankton variability can be attributed to submesoscale eddies that modulate mixed layer stratification and availability of light, resulting in high submesoscale variability in phytoplankton blooms.

1.3.3 Phytoplankton variability in the Sub-Antarctic Zone

In a study of the Southern Ocean seasonal cycle, Thomalla et al. (2011) defined the SAZ as an area that has high chl-a concentrations but has high inter-annual and intra-seasonal variability (low seasonal cycle reproducibility) (see Figure 1.3). They proposed that this variability was likely to be controlled by sub-seasonal forcing of nutrients (iron) and light supply by intra-seasonal physical forcing of the mixed layer (Pasquero et al., 2005). These results led to a study by Swart et al. (2015) in the SAZ that investigated the different forcing mechanism driving variability in upper ocean physics and their effect on sub-seasonal variability of phytoplankton. Their results proposed that differences in inter-seasonal phytoplankton variability (between spring and summer) was driven by different seasonal physical forcing mechanism.

1.3.3.1 Spring

The SAZ is a region where phytoplankton growth is limited by light and not nutrients, particularly in spring. In light limited regions, the spring bloom is typically initiated by surface heating as solar radiation increases. In their study, Thomalla et al. (2011) found that the spring bloom initiation dates in the SAZ had surprisingly high inter-annual variability. They proposed that the variability in spring bloom initiation dates was due to the SAZ's proximity as a region of transition between two different seasonal regimes; the spring bloom of the Sub-Antarctic to the south and the autumn bloom of the Subtropical Zone to the north.

However, the study by Swart et al. (2015) suggested that high feature driven mesoscale variability in the SAZ could drive early (and patchy) bloom initiations and high intra-seasonal phytoplankton variability in spring. In their study, Swart et al. (2015) found that the mixed layer depth (MLD) shoals episodically. This shoaling is driven by the slumping of the lateral density gradient, similar to those observed by Mahadevan et al. (2012) in the North Atlantic. Further analysis found that these periods of enhanced stratification occurred during periods of low wind stress. During these periods of enhanced stratification, the mean light exposure to phytoplankton is increased, and allows for bloom development to occur. As a result, feature-driven restratification acts as hotspots for biological activity when phytoplankton growth is limited by light in spring. A study by Mahadevan et al. (2012) in the subpolar North Atlantic, found that when spring blooms formed by eddy-driven slumping of the density gradient, they formed 20 to 30 days earlier than expected if caused by solar heating alone. As such, Swart et al.

(2015) proposed that the high inter-annual variability in the bloom initiation dates observed in the SAZ was partly due to mesoscale variability and the associated eddy re-stratification that adjusts the annual timing of the spring bloom.

1.3.3.2 Summer

Numerous studies have observed the existence of an elevated and prolonged bloom in summer in the SAZ (Thomalla et al., 2011; Joubert et al., 2014; Carranza and Gille, 2015; Swart et al., 2015). This sustained bloom is somewhat surprising as towards the end of summer, phytoplankton growth is expected to be suppressed by strong iron limitation (Boyd and Ellwood, 2010). A study by Carranza and Gille (2015) found that these sustained summer blooms regularly occur and are widespread across large areas of the Southern Ocean. Furthermore, these sustained summer blooms do not appear to be driven by changes in seasonal forcing. From a glider experiment in the austral summer of 2012-2013, Thomalla et al. (2016) found that the integrated primary production rates were high and fluctuated rapidly (4-6 days) from mid-December to mid-February. These intra-seasonal enhancements in chl-a concentrations where shown to be connected to variations of the MLD in summer (Carranza and Gille, 2015; Swart et al., 2015).

During summer in the SAZ, surface waters are stratified from solar radiation that warms the surface layer. As a result, the mixed layer shoals and phytoplankton are maintained in a high light environment which promotes growth. Swart et al. (2015) found that although the enhanced stratification prevents the deepening of the MLD (to depths > ~80 m), the MLD remains highly variable around a shallow mean depth (~40 m). Their study proposed that variability of the MLD was caused by a combination of the strengthening of the wind stress from synoptic (4 to 9 day) storm events that deepened the MLD, followed by the rapid shoaling of the MLD through the buoyancy of meso- and submesoscale features when the wind stress weakened. A study by Carranza and Gille (2015) supports this theory as their results showed that in summer, strong winds cause the MLD to deepen and in so doing help sustain the chl-a bloom through proposed nutrient entrainment. A study by Joubert et al. (2014) investigated this further and found that in the SAZ in particular, a deepening of the MLD from synoptic storms allows for the entrainment of iron, while the rapid shoaling of the mixed layer allows for phytoplankton growth in a temporary iron replete, high light environment. Nicholson (2016) went on to investigate storm-eddy interactions in the SAZ using a complex physical-biogeochemical model (NEMO-PISCES) and found that storm-eddy dynamics are the primary drivers of the observed variability in phytoplankton in the SAZ in

summer. In addition, these model results showed that storm-eddy interactions allowed for continual resupply of the surface layer with iron to sustain the summer bloom. Therefore, a sustained summer bloom in the SAZ has been proposed to be a result of the combined role of solar heat flux, mesoscale features and synoptic scale storms that alter the mixed layer and in so doing regulate both light and iron supply to the upper ocean at appropriate time scales for phytoplankton growth.

1.4 Sampling platforms

The above studies all highlight the importance of meso and submesoscales of variability (both spatially and temporally) in driving seasonal and sub-seasonal characteristics of phytoplankton variability. However, our knowledge is limited by the difficulties associated with routinely analysing these important scales both in the ocean or with high-resolution models. In the past, the majority of *in situ* ocean research was performed by ships that are unable to observe fine scale changes in phytoplankton biomass and productivity. More recent platforms such as gliders, Argo floats, satellite products and high-resolution models have enabled us to access information at the relevant time and space scales that are necessary for understanding climate sensitivity questions.

Satellites are an effective way in which to monitor the spatial and seasonal variation of global sea surface chl-a (Reilly et al., 1998; Marrari et al., 2006). Satellites provide routine, highly cost-effective synoptic measurements over decadal time scales. In many cases, remotely sensed data are the only regular observations available for frequently under-sampled marine systems such as the polar oceans. Despite the ability of satellites to effectively measure spatial and seasonal variations, problems with remotely sensed data sets do exist. For example, satellites have a course temporal resolution and cloud cover limits ocean colour measurements to a few cloudless days (Moore and Abbott 2000; Marrari et al. 2006; Kaufman et al. 2014). In addition, seasonal measurements in the high latitudes are affected by shortened day lengths and by the large solar angle that occurs during winter months, causing large gaps in satellite chl-a measurements (Moore and Abbott, 2000). Even though satellites have provided high-resolution information on phytoplankton distribution at submesoscales (e.g., Glover et al., 2008), the information is often removed by the averaging of the data into weekly or monthly composites due to the large gaps in the data (Lévy, Iovino, et al., 2012). Another limitation is that satellite ocean colour products are limited to surface observations only. Furthermore, studies have shown that the Southern Ocean's bio-optical relationship between water-leaving radiance and chl-a concentration differs from that at lower latitudes (Mitchell and Kahru 2009; Kahru and Mitchell 2010). These studies have shown

that when Southern Ocean chl-a concentrations are low (≤ 0.1 $mg.m^{-3}$) and high (≥10 $mg.m^{-3}$), the standard algorithm (used for lower latitudes, OC4 for SeaWiFS and OC3m for MODIS) estimates the correct chl-a concentrations but when chl-a concentrations are mid-range (as is the norm) (0.2-2.0 $mg.m^{-3}$) the standard algorithms underestimate chl-a concentrations by 2-3 times compared to *in situ* measurements (Dierssen and Smith 2000; Moore and Abbott 2000; Garcia et al., 2005; Mitchell and Kahru 2009; Kahru and Mitchell 2010). For these reasons, specific bio-optical algorithms need to be developed to retrieve accurate chl-a concentrations for the Southern Ocean that will allow us to better understand phytoplankton variability and long term trends.

Models have allowed us to test our understanding of the physical dynamics and biological coupling of the open ocean. However, accurately parameterising models, especially biological models, is difficult. Of the variety of models run, very few use a high enough resolution to resolve for biogeochemical and physical submesoscale variabilities and when they do, it is both time consuming and computationally expensive. Furthermore, for a model to be informative, it must be forced by observations collected at the appropriate temporal and spatial scales (Niewiadomska et al., 2008). Platforms that adequately sample a region at sufficiently high temporal and spatial resolution are thus needed to assist models in accurately representing phytoplankton variability at meso- and submesoscales.

Traditional ship-based *in situ* measurements allow for spatial variability, but the measurements are limited in time by the duration of the cruise and also depend highly on the weather and other external factors. The ship transects that do occur are short, not repeated enough and are often confined to the austral summer months (Eriksen et al., 2001). Ship-towed devices, such as SeaSoar are however able to sample the ocean at a suitable time resolution that can capture the evolution of submesoscale features due to their speeds of 4 $m\ s^{-1}$ and their ability to repeat a cycle every 3 km in 12 minutes (Rudnick et al., 2004; Lévy, Iovino, et al., 2012). Nonetheless, the cost and demands on research vessels means that these studies remain scarce and short lived, which limits their suitability (Pinot et al., 1995; Niewiadomska et al., 2008; Lévy et al., 2012).

Due to their Eulerian sampling, moorings are able to build up a time series of the effects of meso- and submesoscale variability at a fixed location for long periods of time. However, the problem then arises of how temporal signals in biogeochemistry can be disentangled from simple advection of spatial variability through the site (Lévy, Iovino, et al., 2012). A solution to the lack of spatial variability measurements, would be having a collection of moorings that are spaced at distances that are able to sufficiently

resolve the required spatial variability. However, an approach like this is uneconomical. Even so, a collection of moorings in the Southern Ocean would remain sparse in comparison to the ocean's size (Eriksen et al., 2001). Lagrangian platforms such as floats and drifters provide excellent coverage of temporal and spatial *in situ* measurements. However, they lack the necessary resolution to identify continual meso- and submesoscale features in the upper ocean (Queste et al., 2012) as the floats profile every 10 days and measurements are limited to their parking depth (1000m) (Gould et al., 2004; Roemmich et al., 2004). In addition, float trajectories are determined by currents at depth with the result that they may be advected outside the region of study (Rudnick et al 2004). Purely Lagrangian platforms such as floats also tend to get concentrated into fronts and filaments affecting a bias in their measurements (Senam, 2015).

More recently underwater glider platforms (e.g., SPRAY spray.ucsd.edu/pub/rel/index.php, Slocum www.webbresearch.com/slocumglider.aspx and Seaglider www.irobot.com/gi/maritime/1KA_Seaglider) have been used to collect horizontal and vertical data over a long-time period and at high-resolution (Dickey and Perry, 2008)). Gliders are small, reusable, and relatively inexpensive instruments that can be deployed off small boats. Their high endurance allows them to gather high-resolution observations that span over seasons in hostile oceans, while collecting data across a variety of length scales (Niewiadomska et al., 2008), which traditional sampling platforms (e.g. Ships) have never been able to fully resolve. In addition to the physics, gliders are becoming useful for determining high temporal and spatial resolutions of biogeochemical parameters such as chl-a and carbon (Eriksen et al., 2001). Given the gliders ability to measure continuously, for long periods of time and at high-resolution, these platforms are now able to bridge the gap between the different scales observed thereby creating an effective view of a system's functioning (Queste et al., 2012).

Gliders sample the water column in a sawtooth manner, with pre-set sampling frequencies for the attached CTD and bio-optical sensors. Gliders are propelled through the oceans via a buoyancy control mechanism that is affected by variations in the gliders displaced volume (Eriksen et al., 2001). Each glider is controlled remotely through dead reckoning and GPS location. After each dive cycle, a glider receives instructions via an iridium satellite system that determines its destination. This calculation is based upon the impact of local currents on the glider's previous dive cycle (Frajka-Williams et al. 2009). Due their mobility, gliders can survey transects of up to several thousands of kilometres in length (Queste et al., 2012) and can be directed to monitor a feature that a satellite has identified or a region, which would not normally be possible with a float as it may be advected outside the feature or region by

currents (Rudnick et al., 2004). Gliders can also act as virtual moorings, provided the currents are not stronger than the gliders speed. As a virtual mooring, gliders can provide high-resolution depth profiles, unlike standard moorings with fixed sensors (Rudnick et al., 2004).

Although, gliders have repeatedly proven their advantageous capabilities, there is still uncertainty around this relatively new platform and its associated sampling. Gliders have been found to be restricted by sensor validation, biofouling and battery life (Perry et al., 2008). Slow speeds also mean that strong currents associated with many submesoscale features have the potential to displace gliders, which can result in a failure to capture submesoscale variability (Lévy et al., 2012). Glider missions over the continental shelf are also less efficient than open ocean missions as the depth average currents are smaller, which therefore lessen the physical strain on gliders, while the buoyancy engines are also more efficient at depth (Rudnick et al., 2004). However, a main issue that has been repeatedly raised about gliders is around the interpretation of the data that is collected from a platform that is quasi-Lagrangian in nature. The fact that a glider samples in both time and space makes it difficult to disentangle the role of variability driven by the glider crossing a submesoscale feature in space versus intrinsic changes observed within the water column that are an inherent result of an evolution in time (e.g. phytoplankton growth). Rudnick et al. (2004) proposed that a glider section can confuse temporal variability with spatial structures and therefore that gliders should not be considered as suitable platforms to capture a snapshot of ocean conditions. However, Swart et al. (2015) addressed this issue by looking at the temporal coherence of MLD observations between two gliders. The spatial separation of the two gliders in the SAZ at one time was 213 km apart but their sub-seasonal MLD magnitudes and variability was the same. This supports the fact that both gliders were measuring temporal variability that was being forced by synoptic scale wind forcing. Our aim in this study was to try to determine how much of the surface chl-a variability measured with a glider is the result of temporal variability verses spatial patchiness and to see whether the glider is able to accurately measure the important small scales of variability.

Chapter 2:

Quantifying the significance of temporal scales of phytoplankton variability in the Sub-Antarctic Zone using a high-resolution glider dataset

2.1 Introduction

The Southern Ocean is responsible for 40% of global carbon dioxide (CO_2) uptake (Gruber et al., 2009) and the sub-basin of the Sub-Antarctic Zone (SAZ) is recognized as one of the regions of higher carbon export and an effective atmospheric CO_2 sink (Metzl et al., 1999; McNeil et al., 2001; Trull et al., 2001; Wang et al., 2001). This is primarily due to an efficient solubility pump in combination with the biological pump, which maintains a strong CO_2 sink year round (McNeil et al., 2007). The Southern Ocean seasonal cycle is known for having one of the strongest modes of variability (Monteiro et al., 2011). This is important because the seasonal cycle is the mode through which the physical mechanisms of climate forcing are coupled to ecosystem responses in primary production, diversity and carbon export (Rodgers et al., 2008). Recent studies have found that physical processes at fine spatial scales (meso- to submesoscale) and seasonal to sub-seasonal temporal scales, play an important role in characterising regional variability in the Southern Ocean's seasonal cycle (Thomalla et al., 2011). As such, it is important that we investigate these fine scales so that we are able to understand the sensitivity of Southern Ocean primary production to climate change (Boyd, 2002; Thomalla et al., 2011; Lévy et al., 2012). These fine scale processes are however poorly understood due to the lack of appropriate observations and consequently our understanding of phytoplankton seasonal distribution, rates of production and carbon export is limited, especially in the Southern Ocean.

Satellites are one of the most effective ways in which to monitor the spatial and seasonal variation in global sea surface chlorophyll (chl-a) (Reilly et al., 1998; Marrari et al., 2006). However, problems with ocean colour data sets do exist, mainly due to cloud cover limiting measurements to a few cloudless days. This leads to a tendency for satellite ocean colour data sets to be averaged both in space and time thus reducing their ability to resolve fine scale features (Moore and Abbott, 2000; Marrari et al., 2006; Kaufman et al., 2014). Another method of both spatial and seasonal sampling is through the use of Seagliders, which serve as long-range autonomous platforms providing measurements of the upper ocean at high temporal and spatial resolution (Eriksen et al., 2001; Perry et al., 2008; Frajka-Williams et al., 2009; Swart et al., 2015). However, glider measurements are neither Eulerian nor Lagrangian, which makes interpretation of the space and time scales of variability difficult. Hence, glider sampling requires a more thorough evaluation so that we may better understand their limitations and more effectively interpret the data they provide.

The Southern Ocean Seasonal Cycle Experiment (SOSCEx) was initiated to improve Southern Ocean observations, from primarily ship-based observations to system-scale dynamic studies spanning a much greater range in time and space (Swart et al., 2012). The aim of SOSCEx was to provide a way to better understand the connection between climate drivers, ecosystem productivity and climate feedbacks in the Southern Ocean (Swart et al., 2012). This was approached with the use of five Seagliders, which were distributed between fronts in the Antarctic Circumpolar Current, ship based measurements from the *S.A. Agulhas II,* and satellite measurements. Together, the SOSCEx process study managed to obtain a suite of measurements from the SAZ for austral spring to summer of 2012-2013.

Results from SOSCEx showed that the SAZ was characterised by high sub-seasonal variability in surface chl-a (Swart et al., 2015). As a result of the contrasting characteristics of the upper ocean physics at the beginning versus the end of the glider transect, Swart et al. (2015) separated the data into two distinct periods, the spring bloom initiation phase and the summer sustained bloom phase. During spring, surface chl-a concentrations in the SAZ were intermittent and patchy. This was found to be the result of mixed layer eddies which are meso- and submesoscale features that enhance stratification (thereby increasing the light supply) allowing for the rapid formation of patchy phytoplankton blooms (Swart et al., 2015). In contrast, in summer, solar heat flux, mesoscale features and sub-seasonal storms cause variability of the mixed layer depth (MLD) around a threshold of ~40 m (thereby entraining limiting nutrients), that results in the formation of large homogenous phytoplankton blooms that are sustained throughout summer (Swart et al., 2015).

This study uses the same SOSCEx glider data set that is described above by Swart et al. (2015) to further investigate the spatial and time scales of phytoplankton variability in the SAZ. For this study mesoscales are defined as scales that occur between 10 to 25 days and submesoscales are defined as variability between 2 and 10 days.

Key Questions

A number of recent studies, relying mostly on remotely sensed data or model output, have found that phytoplankton distribution is affected by meso- and submesoscale features (Boyd, 2002; Thomalla et al., 2011; Lévy et al., 2012). However, the extent to which these feature's length and time variability affect phytoplankton is not fully understood. In this study, an Empirical Mode Decomposition analysis of the surface chl-a glider data set in the SAZ is used to address the following key questions:

1. How much of the observed variation in the glider data set can be attributed to seasonal, mesoscale and sub-mesoscale signals?
2. Does the magnitude of phytoplankton variability change seasonally?
3. How do the scales of variability of the physical drivers of wind and MLD compare to those of the surface chl-a time series?
4. If sampled at the dominant scales of variability can you capture the characteristics (mean and standard deviation) of the seasonal cycle?

2.2 Data and methods

2.2.1 SOSCEx glider deployment

The Seagliders used in this study were long range autonomous vehicles, that were originally developed by the University of Washington to provide high temporal and spatial resolution measurements of the upper ocean. Each Seaglider is 1.2 m in length and weighs 52 kg. Seagliders sample the water column in a v-shaped sawtooth pattern from the ocean surface to a programed depth of 1000 m and back to the surface. The gliders move at an average horizontal velocity of 0.33 m s^{-1} and a vertical velocity of 0.1 m s^{-1}, while sampling the water column with pre-set sampling frequencies for the attached CTD and bio-optical sensors. Gliders are propelled by their own buoyancy control effect caused by a variation in displacement of hydraulic oil between internal and external bladders, which results in the glider rising or sinking. The horizontal distance travelled to the target position is determined by the angles of the glider wings. After surfacing from each dive the glider transmits the data and receives a new target location from the base station via an iridium satellite (Eriksen et al., 2001).

As part of SOSCEx, an autonomous Seaglider was deployed in the SAZ during the austral spring to late summer of 2012-2013 from the *S.A. Agulhas II*. On the 25 September 2012 Seaglider 573 (SG573) was deployed in the South East Atlantic Ocean, south of Gough Island at 43.0˚S, 11.0˚W. After continuously sampling the SAZ for 143 days (5.5 months) and covering a distance of 1 693 km, the glider was retrieved on the 15 February 2013 (Figure 2.1).

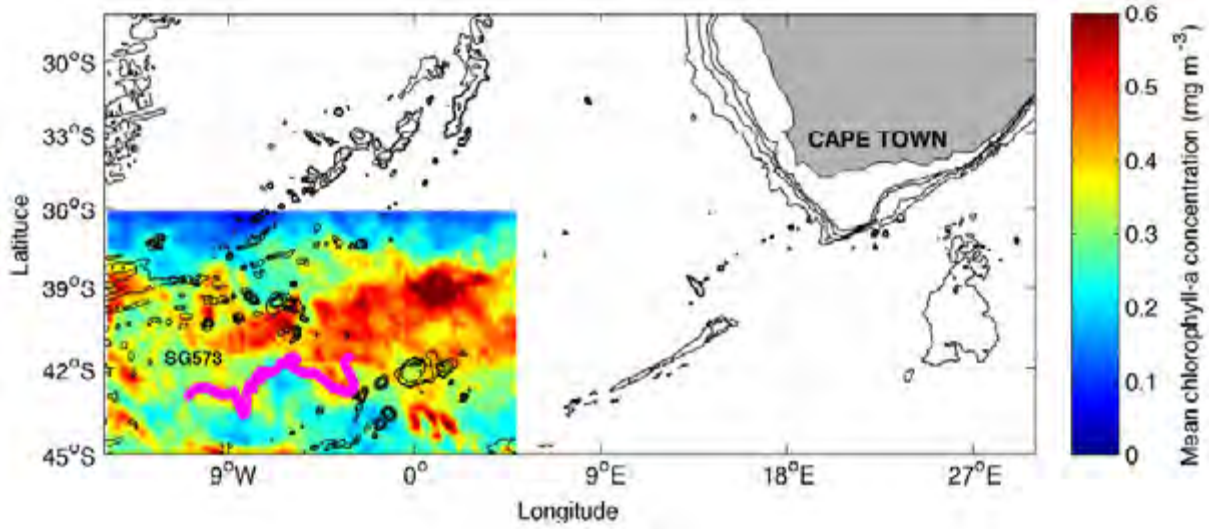

Figure 2.1 Mean satellite chl-a concentrations (mg m^{-3}) during the period of SOSCEx (25 September 2012 – 15 February 2013), with the trajectory covered by Seaglider 573 (SG573) in the magenta line. The bathymetry for the region is overlaid using black contour lines (Figure adapted Swart et al. 2015).

The glider has a suite of sensors that measure CTD (conductivity, temperature and depth), dissolved oxygen, fluorescence (a proxy for phytoplankton concentration), Photosynthetically Active Radiation (PAR) and two wavelengths of optical backscattering Bb(470) and Bb(700) (proxies for particle concentration). The bio-optical sampling rates varied from 0.15 Hz in the upper 100 m to between 0.05-0.1 Hz for the rest of the water column so as to optimize battery performance on longer missions such as these. Each dive cycle took approximately 5 hours and covered an average horizontal distance of 2.8 km, providing a total of 1 212 profiles. This allowed for a temporal resolution of ~2.5 hours and a spatial resolution of ~1.4 km, which enabled both meso- (10-200 km) and submesoscale (1-10 km) features to be sampled. The data was received in real-time via satellite transmission, upon the glider surfacing after each dive.

At the deployment and retrieval of each glider, ship-based CTDs were deployed and samples of chl-a, dissolved oxygen and salinity were collected to calibrate the sensors. From the beginning of January 2013 (the final 5 weeks of the experimental period) the CTD cell was subjected to bio-fouling by Goose-neck barnacles, which affected the quality of the data obtained (Figure 2.2). The barnacle growth is believed to have constricted the flow rate between the temperature and salinity sensors, however there was little impact on the temperature data. In addition, the fluorescence and backscattering data sets were cleaned by removing spikes and bad profiles resulting from sporadic instrument malfunction.

Figure 2.2 Glider covered in Goose-neck barnacles upon recovery from the Southern Ocean, highlighting the bio-fouling issues associated with long deployments.

2.2.1.1 Fluorescence quenching correction and fluorescence to chl-a conversion

Fluorescence and optical backscattering both relate to biological activity and can be used to provide a proxy for phytoplankton biomass in the ocean (Frajka-Williams et al., 2009). Chl-a inside phytoplankton cells has a maximum absorption at 440 nm and a maximum fluorescence at 685 nm (Perry et al., 2008). The unique wavelength of fluorescence and spectral distance between excitation and emission wavelengths makes fluorescence a reliable proxy for phytoplankton biomass. Optical backscattering on the other hand is proportional to the concentration of particles in the water and as such provides a proxy for phytoplankton biomass (when phytoplankton are the primary determinants of the particle field and the contribution by mineral particulates is negligible).

Fluorescence values were dark corrected by subtracting the dark count (calculated as the median fluorescence value below 300 nm). Non-photochemical quenching (NPQ) was present in the fluorescence values, which showed strong light-dependent depressions each day. NPQ is a diurnal cycle of a decrease in fluorescence yield during the day in the surface layer (Buschmann, 1999; Sackmann et al., 2008; Frajka-Williams et al., 2009). NPQ is a manner by which phytoplankton protect themselves against damage from high light intensity. NPQ was corrected by isolating the day time profiles as the time period between the local sunrise and 2.5 hours after local sunset (quenching was still present in the first profile after sunset). The day profiles were corrected using a quenching correction derived from the

optical backscattering (Bb). The correction was based on the methods described in Sackmann et al., (2008) where night time ratios of fluorescence to optical backscattering (Fl:Bb) are relatively constant throughout the mixed layer due to the absence of quenching. During the day however, large decreases in Fl:Bb are observed in the upper surface layer due to quenching. Since both fluorescence and backscattering are proxies for the same phytoplankton biomass, backscattering can be used to correct the quenched fluorescence. This is carried out by calculating the maximum ratio between fluorescence and backscattering Fl:Bb(700) per profile and multiplying this ratio with Bb(700) from the depth of maximum Fl:Bb(700) to the surface to get corrected fluorescence. In 16.8% of the data sets where Bb(700) was found to be corrupt due to intermittent electronic fluctuation, Fl:Bb(470) was used instead. On the rare occasions when both Bb(700) and Bb(470) where absent, a well-mixed layer was assumed and the fluorescence was corrected by extrapolating the maximum fluorescence value from the depth of maximum fluorescence to the surface (Xing et al., 2012).

These methods, assume that there is a constant carbon to chlorophyll ratio throughout the surface waters and that phytoplankton do not exhibit a photo adaptive strategy by changing the amount of chl-a present in a cell as they are mixed deeper in the water column. Regions characterised by a deep fluorescence maximum (e.g. North Sea)(Fernand et al., 2013) do not conform to this assumption, making this method inappropriate in those areas. In the Southern Ocean however, the well mixed surface waters and the absence of deep fluorescence maxima (as seen from the non-quenched night time profiles), makes this assumption acceptable and the quenching corrections reliable.

On glider deployment and retrieval, *in situ* chl-a bottle samples were collected from six depths from each coincident CTD. Samples of 250 ml were filtered onto 25mm GF/F Whatman filters and extracted in 8 ml of 90% acetone for 24 hours at -20˚C. A Turner Trilogy Laboratory Fluorometer, calibrated with a pure chl-a standard, was used to measure the chl-a concentrations ($\mu g\ l^{-1}$). Glider fluorescence was converted to chl-a using the instrument specific chl-a conversion factor supplied by the manufacturer. This was due to the limited number of collocated samples per glider (12), which meant that the regression between *in situ* chl-a and glider fluorescence would not be statistically robust (Swart et al., 2015). The conversion allowed for the 83 collocated glider chl-a and *in situ* chl-a samples from all five SOSCEx gliders to be plotted simultaneously to form a statistically significant regression (slope = 4.12, intercept = -0.21, r2 = 0.66). To correct for the manufacturer conversion to chl-a, the slope of the regression was applied to all glider chlorophyll measurements to obtain chl-a measurements that were

more suited to the regional characteristics of the Southern Ocean (For more details see Swart et al., 2015).

2.2.1.2 Backscattering to phytoplankton carbon conversion

Stramski et al. (1999) noted a relationship between phytoplankton carbon (C_{phyto}) and backscattering (Bb) as a result of the dominant organic particular concentration that controls the changes in both particular organic carbon (POC) and particulate backscattering (b_{bp}).

A seven point running median filter was used to separate the spikes from the glider backscattering (λ=470 and 700) data (Briggs et al., 2011). The glider Bb was then converted into particular backscattering using the models of Zhang and Hu (2009) and Zhang et al. (2009).

$$\mathrm{b_{bp}} = 2\pi\chi_p[\mathrm{S(Bb - D)} - \beta_{sw}] \quad (2.1)$$

Where χ_p is equal to 1.1 and is the factor used to convert β_p (at a central angle of 117˚) to β_{bp} (Boss & Pegau, 2001); S is the instrument specific scaling factor; Bb are the digital count (λ=470 and 700) and D the dark count; β_{sw} is the volume of scattering of pure water. The remaining spikes in the b_{bp} were removed with a threshold in shallow (b_{bp}>0.048) and deep (b_{bp}>0.0025) waters. Profiles with a high mean backscattering (b_{bp}>0.001) in deep waters (>150m) were discarded (see Thomalla et al., 2016 for further details).

The POC was calculated from b_{bp} using a linear regression between POC and $\mathrm{b_{bp}}$ (Thomalla et al., 2016) and a mean ratio between total POC and phytoplankton specific carbon (C_{phyto}) of 30% (Behrenfeld et al., 2005). In total 221 POC samples from CTDs from a number of cruises in the Southern Ocean were plotted against collocated b_{bp}470 and linearly correlated to provide a regionally specific regression to convert b_{bp}470 into POC (Thomalla et al., 2016).

$$\mathrm{POC} = 32057 \times \mathrm{b_{bp}} + 2.6 \quad (2.2)$$

POC however still needs to be converted into a fraction specific to phytoplankton (C_{phyto}). Behrenfeld et al. (2005) summarized ranges of field based C_{phyto}:POC ratios from different oceanic regions to an average phytoplankton contribution to total particulate organic carbon of ~30%. As such, POC was converted into C_{phyto} according to the following equation that converts b_{bp} into POC using a linear

regression and then uses a constant 30% fraction to represent C_{phyto} (see Thomalla et al., 2016 for more details).

$$\mathrm{Cphyto} = 0.3\left(32057 \times \mathrm{b_{bp}} + 2.6\right) \quad (2.3)$$

2.2.2 Satellite products

2.2.2.1 Wind stress

The wind data used in this study was obtained from a SeaWinds blended vector sea surface wind (at 10 m above seas level reference height) product. This product combines observations from multiple satellites (microwave, radiometer and scatterometer sensors) to produce a global 6-hourly, 0.25˚ resolution, gridded product (Zhang et al., 2006). The wind data was collocated with the gliders in space and time using a 2-dimensional bilinear interpolation and converted from wind speed into a wind stress product using the Large and Pond (1981) method (du Plessis, 2014; Swart et al., 2015).

2.2.2.2 Mixed layer depth

The MLD was calculated using (de Boyer Montegut et al., 2004) temperature criteria where a change in temperature of 0.2˚C from the reference depth of 10 m denotes the MLD. The reason this method was used was due to thermal lag errors and biofouling of the glider which introduces errors in glider salinity measurements. A recent study with this data set successfully applied this criterion of $\Delta T = 0.2^{\circ}C$ (Swart et al., 2015) to correct for these errors.

2.2.3 Temporal analysis

2.2.3.1 Empirical Mode Decomposition

Empirical Mode Decomposition (EMD) is a function that decomposes a signal from data into primary signals called Intrinsic Mode Functions (IMFs) (Rato et al., 2008). IMFs represent modes of oscillation entrenched in the data. EMD performs a spectral analysis using Hilbert transforms, which is followed by an instantaneous frequency computation (Huang et al., 1998). EMD is a single band filter, where the EMD calculations are based on Rato et al. (2008). The MATLAB function *rParabEmd__L*. EMDs was used to find temporal signals that were embedded within the surface chl-a data set. Wind stress, MLD and

POC were similarly decomposed to allow a comparison of their modes of temporal variability with that of surface chl-a from the IMFs.

Huang et al. (1998) proposed EMD as a signal decomposition algorithm based on the successive removal of an elemental signal, the IMFS. Given any signal x(t), the IMFs are found by an iterative procedure called sifting algorithm, which is composed of the following steps:

1) Find all the local maxima, M_i, $i = 1,2, \ldots$, and minima, m_k, $k = 1,2, \ldots$, in $x(t)$.
2) Compute the corresponding interpolating signals $M(t) := f_M(M_i, t)$, and $m(t) := f_k(m_i, t)$ These signals are the upper and lower envelopes of the signal.
3) Let $e(t) := (M(t) + m(t))/2$.
4) Subtract e(t) form the signal: $x(t) := x(t) - e(t)$.
5) Return to step (1) – stop when $x(t)$ remains nearly unchanged.
6) Once we obtain an IMF, $\varphi(t)$, remove it from the signal $x(t) \coloneqq x(t) - \varphi(t)$ and return to (a) if $x(t)$ has more than one extremum (neither a constant nor a trend).

The temporal mode of variability for each IMF was calculated by averaging the time between the peaks and troughs of each IMF. The EMD analysis was performed over the entire data set and for each individual season (spring and summer) of glider deployment.

2.2.3.2 Statistical analysis of temporal modes of variability

A low pass filter that used a running mean was used to confirm the precision with which the IMFs were identified by the EMD. The signals identified by the EMD were consistent yet superior to the low pass filter as the EMD was able to identify specific signals of both high and low frequencies. Correlation statistics were used to determine how well each IMF signal explained the temporal variability of each variable (surface chl-a, MLD, wind stress and POC) and its significance to the sub-seasonal variability of the variable. The percentage of variance explained, analysed separately for each IMF, was computed by analysing the linear relationship between the IMF and the original data set. The combined estimates of variance explained by the meso- and submesoscales was recomputed by analysing the linear relationship between the combined IMFs and the original data set. All combined estimates stated in the results and discussion show the recomputed percentages.

In order to test the robustness of the dominant scales of temporal variability, subsamples at these scales (set frequencies) were taken from the data set at random starting times. The subsampling occurred at half the time period of each dominant frequency to capture the periodicity of the frequency. For each time series, only the full number of subsampling extractions were taken. For further robustness, this was repeated by randomly subsampling the time series with the same number of extractions used in the equivalent set frequency subsampling. This was repeated for the same number of times as the equivalent set frequencies subsampled the time series. The mean, standard deviation and root mean square error (RMSE) of the standard deviation of the subsampled time series (set frequency and purely random) was compared to that of the original high resolution time series of surface chl-a and the random extractions. The mean, standard deviation and RMSE were compared to the original data set to establish whether sampling of surface chl-a needs to occur at the dominant frequency in order to capture the multi-seasonal characteristic observed in phytoplankton. This was repeated for both spring and summer.

2.3 Results

2.3.1 Seasonal distribution of surface chl-a

Over the 5.5 month period of glider deployment, surface chl-a concentration ranged from 0.16 to 1.34 mg m^{-3}. The surface chl-a concentration remained relatively low in spring (mean = 0.38 mg m^{-3}), ranging between 0.16 and 0.80 mg m^{-3}. In early October there was a slight increase in surface chl-a concentration that lasted less than a week, before dropping. From the beginning of November surface chl-a concentrations increased rapidly as the water column underwent a transition from spring to summer, becoming more favourable for phytoplankton growth. Summer surface chl-a concentrations remained relatively high (mean = 0.78 mg m^{-3}), with large oscillations between 0.35 mg m^{-3} and 1.34 mg m^{-3} (Figure 2.3).

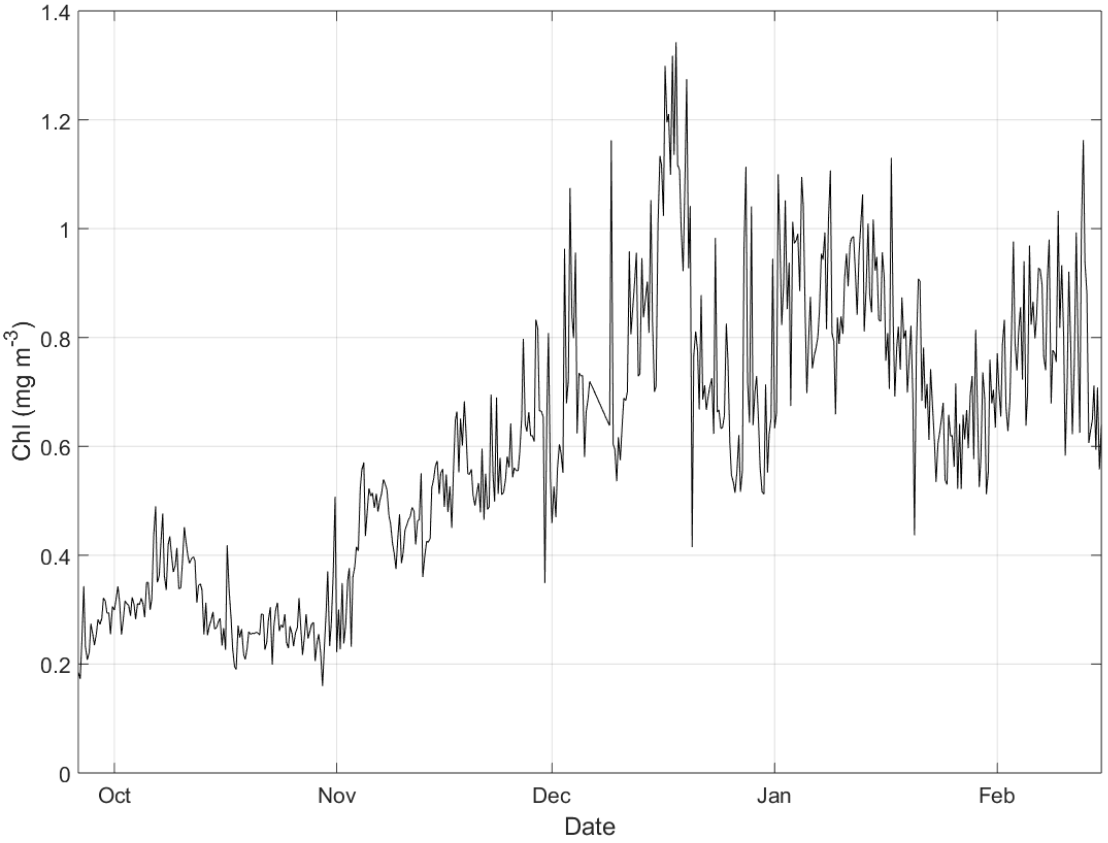

Figure 2.3 Surface chl-a concentrations (mg m^{-3}) obtained from SG573 deployed in the Southern Ocean between 25 September 2012 to 15 February 2013.

2.3.1.1 Sub-seasonal variability of surface chl-a

An Empirical Mode Decomposition (EMD) was carried out on the entire surface chl-a time series in order to decompose the dataset into sub-seasonal temporal signals. The EMD was able to identify nine distinct Intrinsic Mode Functions (IMF) within this time series. The temporal modes of variability identified ranged from diurnal to multi-seasonal scales (Figure 2.4). The dominant mode of variability was the multi-seasonal signal, which explained 58% of the surface chl-a variability. In order to investigate whether there was a seasonal difference in the dominant scales of variability the data set was then separated into spring and summer for further EMD analysis. The transition date (28th of November 2012) was determined according to Swart et al. (2015) as the date of transition between different physical and biochemical properties that characterised spring and summer.

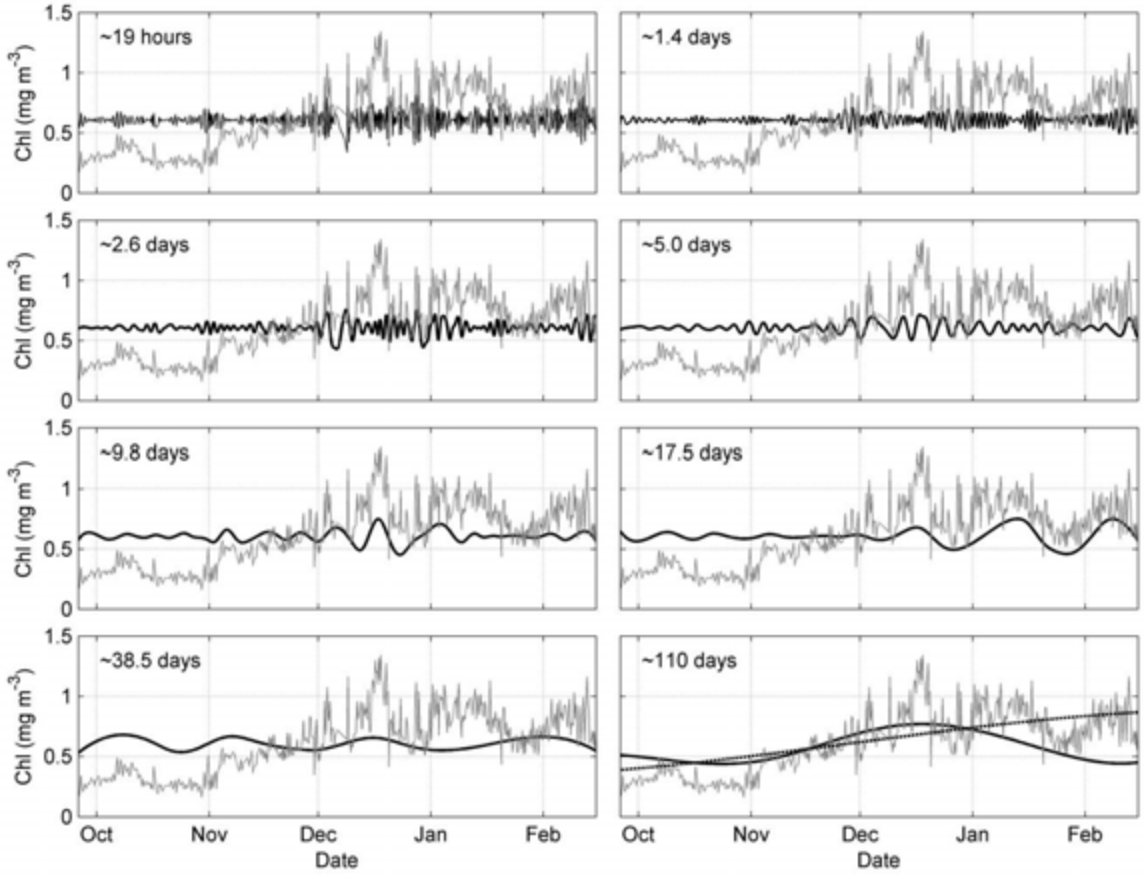

Figure 2.4 Empirical Mode Decomposition of the multi-seasonal surface chl-a time series. Eight different modes of variability (IMFs) in black and the residual IMF (dotted black line) were identified by the EMD from the surface chl-a time series (grey line).

An EMD conducted over the spring period identified 7 IMFs embedded within the time series, while 8 IMFs were identified within the summer time series (Table 2.1). The dominant signal in spring was the

residual (multi-seasonal) signal which explained 79% of surface chl-a variance. The next dominant temporal signal was a 20 hr daily signal, that explained 9% of surface chl-a temporal variability. Although the EMD detected meso- and submesoscale temporal signals (IMF 3-IMF 5), none of these signals were significant. In contrast to spring, the residual signal was not a dominant signal in summer, but rather the daily (~18hrs), and 17.5 day signals where dominant. These signals each explained 22% of surface chl-a variability in summer. Over the summer period, submesoscales of temporal variability (~7 and ~5 days) were significant and together explained 19% of surface chl-a variability.

IMF	Multi-seasonal	Spring	Summer
1	0.8 (7%)	0.8 (9%)	***0.8 (22%)***
2	1.4 (3%)	1.7 5%)	1.3 (10%)
3	2.6 (2%)	3.0 (3%)	2.6 (9%)
4	5.0 (4%)	5.3 (1%)	4.5 (11%)
5	9.8 (4%)	8.5 (1%)	7.8 (2%)
6	17.5 (9%)	16.1 (5%)	***17.5 (22%)***
7	38.5 (0%)	***Residual (79%)***	30.6 (14%)
8	110 (34%)		Residual (5%)
9	***Residual (58%)***		

Table 2.1 Temporal modes of variability (days) and the respective square of the correlation (r^2) defining the variance for each of the IMFs calculated for the full multi-seasonal time series of surface chl-a as well as for the separation of the time series into spring and summer. The dominant signal is in bold italics, the submesoscales are highlighted in green, while all modes of variability that are not significant above the 99%, are highlighted in grey.

Each IMF signal identified from the EMD was validated with the use of a low pass filter, which uses a running mean, at the temporal periods identified by the EMD. Although the signals identified by the EMD were consistent with those of the low pass filter (Figure 2.5), the EMD was superior as it was able to identify specific signals of high and low frequencies.

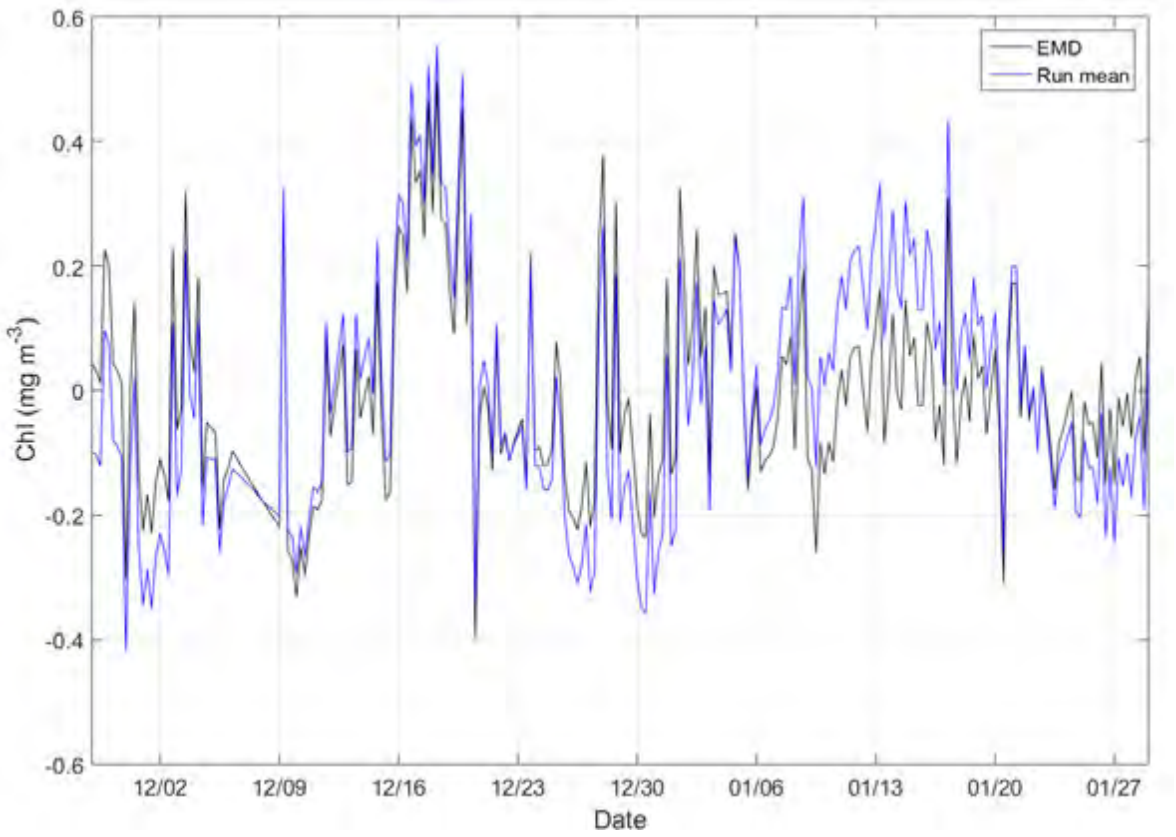

Figure 2.5 The IMF (black line) and low pass filter (blue line) of the dominant 17.5 day signal identified by the EMD for the summer time series of surface chl-a.

Multi-seasonal and daily signals were masking the effects of sub-seasonal scales of temporal variability, which are the primary interest of this study. As such, the full multi-seasonal data set as well as the separated spring and summer time series underwent a low pass filter (daily running mean) to remove the dominant daily signal from the time series that was dampening the signal of meso- and submesoscales of variability. Similarly, the dominant multi-seasonal signal was removed from the spring and summer series by removing the EMD residual from each season's time series. An EMD analysis carried out on the modified times series, was able to detect 9 IMFs from the full multi-seasonal time series with 8 and 7 IMFs embed within the spring and summer time series, respectively (Table 2.2). Looking at the full time series, the mesoscale signal of 15.4 days dominated with 29%, while the submesoscales (~2, ~5 and ~8 days) together accounting for 30% of the variability. In spring, the EMD analysis showed that the IMF data was dominated by the ~10 day signal (51% of surface chl-a variability), with the remaining submesoscale signals (~2 and ~5 day) accounting for 4% and 33% of surface chl-a variability, respectively. As such, the combined submesoscales dominated the variability in spring (97%). The removal of the daily and multi-seasonal signal shifted the dominant signals observed

in summer to a single monthly (~27 days) signal (54% of chl-a variability), while submesoscales (~2, ~4 and ~9 days) of variability increased to explain a joint estimate of ~27% of the observed variability (see Section 2.2.3.2).

IMF	Multi-seasonal	Spring	Summer
1	0.8 (1%)	0.8 (2%)	0.8 (1%)
2	2.2 (9%)	2.1 (4%)	2.2 (10%)
3	4.8 (15%)	4.8 (33%)	4.2 (19%)
4	8.7 (10%)	***9.9 (51%)***	8.9 (6%)
5	***15.4 (29%)***	14.8 (2%)	***27.1 (54%)***
6	28.9 (2%)	22.0 (0%)	62.5 (0%)
7	38.0 (8%)	40.0 (0%)	Residual (4%)
8	64 (3%)	Residual (0%)	
9	Residual (4%)		

Table 2.2 Temporal modes of variability (days) and the respective square of the correlation (r^2) defining the variance for each of the IMFs calculated for the full multi-seasonal time series of surface chl-a as well as for the separation of the time series into spring and summer with the daily and multi-seasonal signal removed. The dominant signal is in bold italics, the submesoscales are highlighted in green, while all modes of variability that are not significant above the 99%, are highlighted in grey.

2.3.1.2 Subsampling

Subsampling of the glider surface chl-a time series at the dominant scales of variability was performed to test whether the dominant frequencies found with the EMD analysis could accurately capture the same mean and variance observed in the high-resolution 6 hourly time series. The spring surface chl-a time series was subsampled at the two dominant submesoscale periods, ~5 and ~10 days (33 and 51% respectively, Table 2.2). Two subsampling approaches were used: 1) the time series was sampled with a set of extractions with a constant period (~5 and ~10 days) and a random starting point and 2) instead of subsampling at systematic intervals (which is seldom possible with platforms such as satellites due to cloud cover), the subsampling was also performed with a random selection of data points (that totalled the same number of data points as in approach 1) but with no periodicity.

The mean and standard deviation for the subsampled ~5 day data set (0.38 mg m^{-3} and 0.12 mg m^{-3}, respectively) using set frequency sampling was very similar to the mean and standard deviation of the high-resolution spring time series (Figure 2.6). The mean (0.39 mg m^{-3}) and standard deviation (0.13 mg m^{-3}) of the 10 day subsampled time series was slightly higher than the high-resolution spring time series. The standard deviations increased for both subsampled data sets due to a shift in starting points into spring (further up the multi-seasonal ramp) and hence give higher mean surface chl-a readings. Worth

noting is that the standard deviation of the 10 day subsampled time series deviated further from the mean of the high-resolution time series than the standard deviation of the 5 day subsampled time series. Purely random extractions (with no periodicity) on the other hand produced means (0.39 mg m^{-3} for both ~5 and ~10 day extractions) that were slightly higher than the spring mean (0.38 mg m^{-3}; Figure 2.6 a,b). In addition, the standard deviation of the purely random extraction for both subsamples was highly variable, especially for the ~10 day random extraction. To summarise; with respect to both the mean and standard deviation, the higher the subsampling frequency (shorter period) the less the error in predicting the mean of the original spring time series.

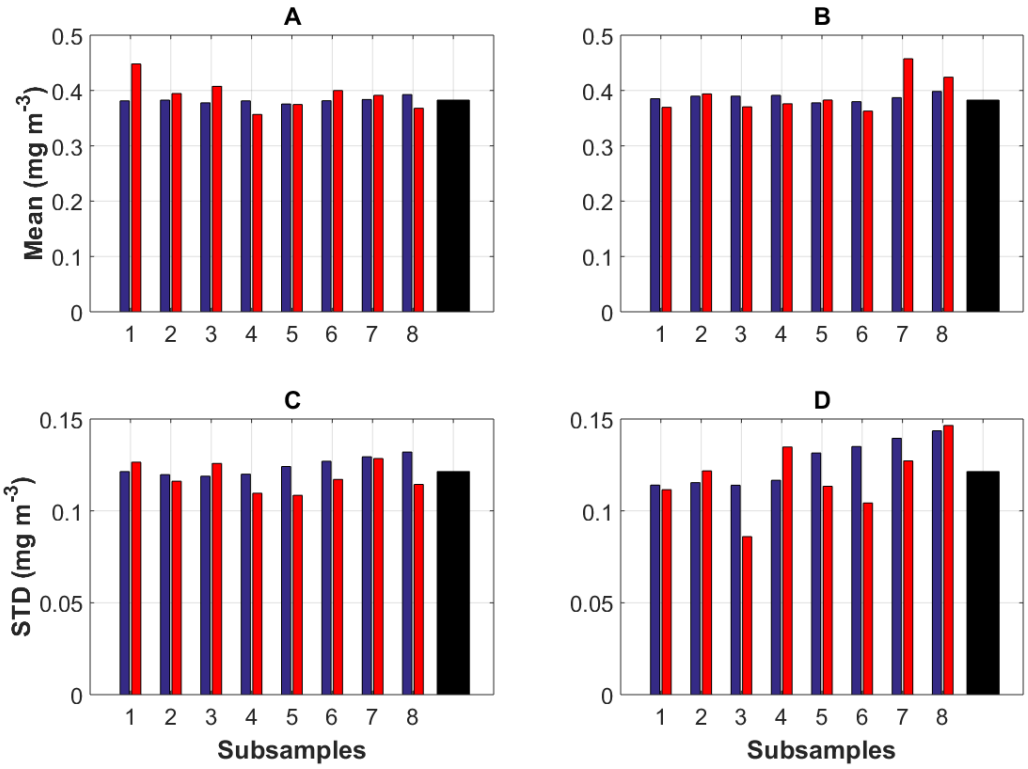

Figure 2.6 The mean and standard deviation of the ~5 day (A and C) and ~10 day (B and D) subsampling (blue bar) and the corresponding random extraction (red bar) for spring surface chl-a, respectively. The full spring time series mean and standard deviation is black.

The three dominant signals observed in summer were similarly used to subsample the summer time series, the two submesoscale signals (~4 and ~9 days) and the dominant monthly signal (~27 days). The means of the ~4 and ~9 day subsamples at set frequencies (0.78 mg m^{-3}, for both) were the same as the high-resolution summer time series (0.78 mg m^{-3}) (Figure 2.7 a,b). The mean for the 4 day random extraction (0.76 mg m^{-3}) was lower than the high-resolution summer time series, while the 9 day random extraction mean (0.79 mg m^{-3}) was slightly higher. The ~4 day subsampling frequency standard

deviation (0.14 mg m^{-3}) was also the same as the high-resolution summer time series (0.14 mg m^{-3}), however both the ~4 and ~9 day subsampling standard deviations increased and then decreased as the starting points shifted into summer (Figure 2.7 d,e). The mean (0.73 and 0.76 mg m^{-3}, respectively) of the ~27 day subsamples (at both set frequency and random) was less than that of the high-resolution time series, however the standard deviations were different. The standard deviation for the set frequency subsample was lower (0.06 mg m^{-3}) than the high-resolution summer time series (0.14 mg m^{-3}) while the standard deviation from the random subsampling was much more variable (0.08 to 0.18 mg m^{-3}). In summary and similar to in spring, the higher subsampling frequency (~4 and ~9 days) had less error in predicting the summer time series, while the lower subsampling frequencies (~27 days) underestimated the original summer surface chl-a time series in respect of both mean concentration and variability.

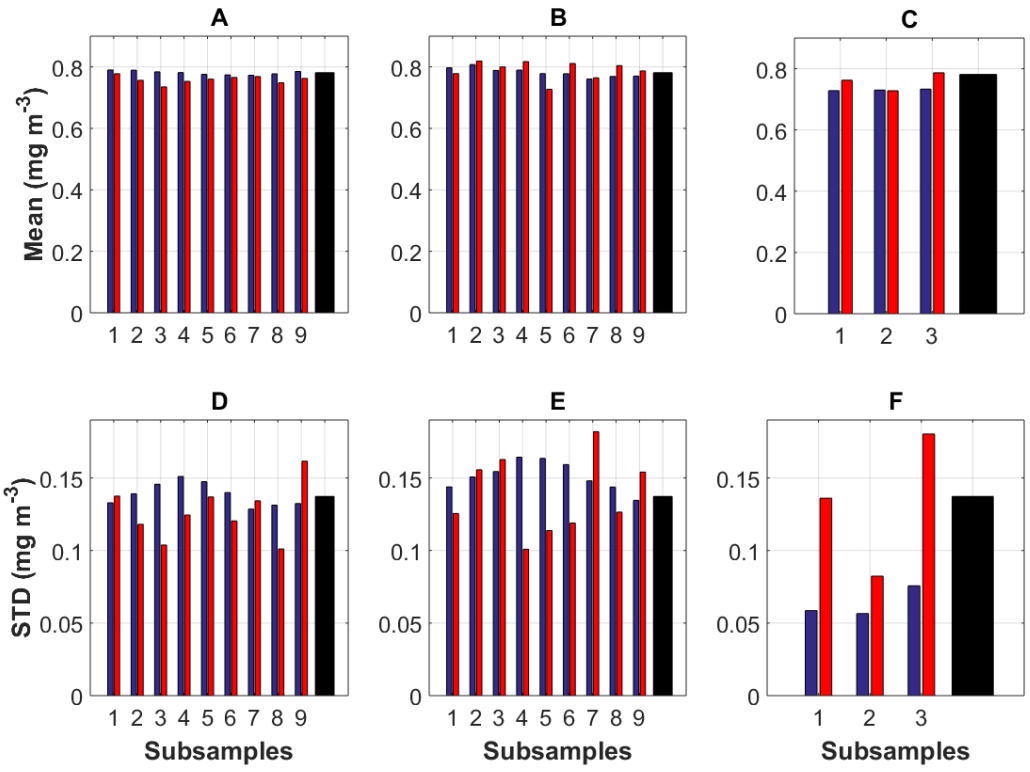

Figure 2.7 The mean and standard deviation of the ~4 day (A and D), ~9 day (B and E) and ~27 day (C and F) subsampling (blue bar) and the corresponding random extraction (red bar) for summer surface chl-a, respectively. The full summer time series mean and standard deviation is black.

2.3.2 Sub-seasonal MLD and wind stress variability

2.3.2.1 Seasonal

To investigate if there was a multi-seasonal (spring and summer together) relationship between two of the primary drivers of surface chl-a variability in the SAZ, wind stress and MLD were correlated against surface chl-a. multi-seasonal correlations of wind stress and MLD to the surface chl-a time series were both negative, with a very low correlation between surface chl-a and wind stress (r = - 0.06), and a relatively strong correlation (r = - 0.5) between surface chl-a and MLD. To compare the dominant scales of variability, EMD analysis was carried out on both the MLD and wind stress time series. The EMD analysis obtained 7 IMFs embedded in the MLD time series and 8 IMFs in the wind stress time series (Table 2.3). The ~22 day and residual signals described the majority of the MLD variability (27% and 24%, respectively). Combined the submesoscale signals (IMF 2 to IMF 4) describe the equivalent amount of temporal variability (28%) of the MLD. Although the residual signal for wind stress was not significant, the dominant mode of variability returned a low frequency of ~47 days (24% of wind stress variability). Nevertheless, the meso- and submesoscale signals (IMF 2 to IMF 4) of wind stress together explained the majority (58%) of the variability of multi-seasonal wind stress.

IMF	MLD	Wind Stress
1	0.8 (0%)	1.0 (2%)
2	2.2 (6%)	3.2 (8%)
3	5.0 (9%)	7.3 (21%)
4	9.4 (14%)	10.6 (14%)
5	***22.3 (27%)***	19.9 (15%)
6	38.9 (8%)	***47.3 (24%)***
7	Residual (24%)	98.8 (2%)
8		Residual (1%)

Table 2.3 Temporal modes of variability (days) and the respective square of the correlation (r^2) defining the variance for each of the IMFs calculated for the multi-seasonal (spring and summer) MLD and wind stress time series with the daily and multi-seasonal signal removed. The dominant signal is in bold italics, the submesoscales are highlighted in green, while all modes of variability that are not significant above the 99%, are highlighted in grey.

2.3.2.2 Spring

A comparison between the surface chl-a and wind stress time series in spring resulted in a weak positive correlation (r = 0.2), whereas between the MLD and surface chl-a time series there was a weak negative correlation (r = - 0.3). The spring wind stress and MLD were decomposed into 6 IMFs and 7 IMFs,

respectively (Table 2.4). Submesoscale signals appeared to be common modes of temporal variability between MLD, wind stress and surface chl-a in spring. However, the dominant ~3 week signal for both MLD (19.5 days at 34%) and wind stress (22.3days at 21%) was not significant in surface chl-a (Table 2.2). The remaining modes of variability for MLD was the submesoscale temporal signals (~2 to ~7 days) that combined to account for (44%) of the spring variability. While for wind stress, the submesoscale signals (~2 to ~8 days) accounted for the majority of the wind stress variability in spring (47%).

IMF	MLD	Wind Stress
1	0.9 (1%)	1.0 (2%)
2	2.1 (10%)	2.5 (7%)
3	4.2 (17%)	4.4 (12%)
4	7.0 (26%)	8.2 (15%)
5	***19.5 (34%)***	***22.3 (21%)***
6	30.5 (7%)	Residual (3%)
7	Residual (6%)	

Table 2.4 Temporal modes of variability (days) and the respective square of the correlation (r^2) defining the variance for each of the IMFs calculated for the spring MLD and wind stress time series with the daily and multi-seasonal signal removed. The dominant signal is in bold italics, the submesoscales are highlighted in green, while all modes of variability that are not significant above the 99%, are highlighted in grey.

2.3.2.3 Summer

The correlation for both MLD and wind stress to surface chl-a in summer was weak ($r < 0.2$). The EMD analysis was able to identify 6 IMFs and 7 IMFs embedded in the MLD and wind stress time series, respectively (Table 2.5). In both MLD and wind stress time series the dominant mode of variability is the ~weekly signal (6.1 and 5.6 days) which describes 41% and 45% of the variability respectively. The meso- and submesoscale signals were similar between the three time series. The dominant submesoscale signals explained 54% and 92% of the temporal variability experienced by the MLD and wind stress time series over summer. The MLD time series had a third mesoscale signal (~14 day) that accounted for 32% of the variability in summer.

IMF	MLD	Wind Stress
1	0.8 (2%)	1.0 (1%)
2	2.3 (21%)	3.0 (32%)
3	***6.1 (41%)***	***5.6 (45%)***
4	13.9 (32%)	10.2 (28%)
5	45.5 (8%)	19.5 (9%)
6	Residual (0%)	38.8 (0%)
7		Residual (0%)

Table 2.5 Temporal modes of variability (days) and the respective square of the correlation (r^2) defining the variance for each of the IMFs calculated for the summer MLD and wind stress time series with the daily and multi-seasonal signal removed. The dominant signal is in bold italics, the submesoscales are highlighted in green, while all modes of variability that are not significant above the 99%, are highlighted in grey.

2.4 Discussion

The SAZ is a region that is known for having high levels of primary production, where phytoplankton blooms fix large amounts of carbon into the ocean making the SAZ an important zone for the global carbon cycle. The phytoplankton blooms that occur over a multi-seasonal cycle in the SAZ, vary temporally and spatially as a result of different forcing mechanisms occurring in spring and summer (Swart et al., 2015). Our limited understanding of this variability impacts our ability to predict the sensitivity of the carbon cycle to climate change. Investigating the temporal and spatial variability of phytoplankton blooms therefore has significant implications, not only for the understanding of primary production variability, but also in terms of being able to predict the impact of the changing climate on carbon uptake and export. Although recent studies emphasise the importance of meso- and submesoscale features on phytoplankton blooms (Boyd, 2002; Fauchereau et al., 2011; Thomalla et al., 2011; Lévy et al., 2012), little research occurs in this region due to traditional mechanisms (e.g. ships) that are unable to observe fine scale changes in phytoplankton biomass and productivity. More recent platforms such as gliders have enabled us to sample at the relevant time and space scales that are necessary for understanding climate sensitivity questions. However, a better understanding of gliders limitations is required, specifically about how best to interpret the nature of the quasi-Lagrangian time series that is capturing both temporal and spatial scales of variability that are intrinsic to growth and spatial distribution. This study uses a comprehensive data set obtained from the SOCCEx Seaglider deployment in the Atlantic SAZ to investigate the scales of variability that characterise the phytoplankton seasonal and sub-seasonal cycle and to determine the extent to which a glider is able to capture them.

2.4.1 Seasonal and sub-seasonal variability

The SAZ is a typically high biomass region that has a strong seasonal cycle with low surface chl-a in winter, ramping through spring to high surface chl-a in summer. According to a study by Thomalla et al. (2011) that characterised the seasonal cycle according to both biomass and seasonal cycle reproducibility, the SAZ can be separated into two different seasonal regimes (see Figure 1.3). The first regime has high seasonal cycle reproducibility (low inter-annual seasonal variability) as a result of surface chl-a being driven by the predictable seasonal forcing of light, heat flux and seasonal MLD. The second regime has low seasonal cycle reproducibility (high inter-annual and intra-seasonal variability) that is likely driven by sub-seasonal physical forcing of the iron and light supply (Thomalla et al., 2011).

The results from this study confirm that in the SAZ the multi-seasonal scale is the dominant signal in surface chl-a variability over the 5.5 month period of glider deployment, explaining 58% of the temporal variability of surface chl-a (Table 2.6). This is to be expected, as the SAZ, like much of the Southern Ocean, is a region where strong seasonal changes in solar radiation influence the MLD, nutrient and vertical light supply and the subsequent seasonal distribution of phytoplankton production and biomass (Sverdrup, 1953; Boyd et al., 1999; Boyd, 2002; Arrigo et al., 2008).

In addition to the multi-seasonal signal, a dominant daily signal in surface chl-a was observed (20 hours at 7% for the full multi-seasonal time series, 9% for spring and 22% for summer in Table 2.1). The daily signal could be the result of physiological adjustments of the phytoplankton to their day/night light environment (i.e. adjustments in their cellular chl-a:C_{phyto} ratios) or to a residual impact of an imperfect quenching correction applied to daytime chl-a (see Section 2.2.1.1). These possibilities were investigated by applying the EMD to C_{phyto}, as an alternate indicator of phytoplankton biomass that is independent of chl-a (i.e. it is independent of physiological adjustments in diurnal chl-a concentrations that are not linked to biomass or to quenching). When applied to C_{phyto} the EMD analysis presented a similar daily signal (19 hours and 21 hours for spring and summer both at 6%) suggesting that there is also a daily adjustment in phytoplankton carbon. As such, it is believed that the daily signal is a real response of the phytoplankton community, which elicits further detailed investigations that are outside of the scope of this thesis.

IMF	Original	Removed Daily	Removed Multi-seasonal
1	0.8 (7%)	0.8 (0%)	0.8 (1%)
2	1.4 (3%)	2.2 (1%)	2.2 (9%)
3	2.6 (2%)	4.5 (4%)	4.8 (15%)
4	5 (4%)	8.2 (3%)	8.7 (10%)
5	9.8 (4%)	12.7 (4%)	***15.4 (29%)***
6	17.5 (9%)	24.7 (7%)	28.9 (2%)
7	38.5 (0%)	36.4 (0%)	38.0 (8%)
8	110 (34%)	***Residual (78%)***	64 (3%)
9	***Residual (58%)***		Residual (4%)

Table 2.6 Temporal modes of variability (days) and the respective square of the correlation (r^2) defining the variance for each of the IMFs calculated for the original multi-seasonal (spring and summer) surface chl-a time series and the multi-seasonal time series with the daily signal removed and a multi-seasonal time series with both the daily and multi-seasonal signals removed. The dominant signal is in bold italics, the submesoscales are highlighted in green, while all modes of variability that are not significant above the 99%, are highlighted in grey.

Nonetheless, as the multi-seasonal and daily signals masks our ability to adequately observe the sub-seasonal temporal signals which recent studies have found to be important (Boyd, 2002; Fauchereau et al., 2011; Thomalla et al., 2011; Lévy et al., 2012; Swart et al., 2015). These dominant signals were removed. In addition, the time series was spilt into spring (25 September to 28 November) and summer (29 November to 15 February) based on known differences in the inter-seasonal physical forcing mechanisms that drive surface chl-a variability in the SAZ (Swart et al., 2015).

2.4.1.1 Spring temporal variability

The occurrence of phytoplankton blooms in spring is thought to be heterogeneous as they coincide with enhanced horizontal gradients associated with eddies (Mahadevan et al., 2012; Swart et al., 2015), which act as small scale drivers of phytoplankton variability in both space and time. From September to early November, surface chl-a concentrations are generally low (~ 0.25 mg m^{-3}), except at episodic instances of MLD shoaling from eddies or filaments that drive increased concentrations of surface chl-a (~ 0.4 mg m^{-3}) (Swart et al., 2015) (see Figure 2.3). Although the correlation between MLD and surface chl-a was negative i.e. shallow MLD's tended to coincide with higher surface chl-a concentrations (and vice versa), the correlation was weak (r = - 0.3).

IMF	Surface chl-a	MLD	Wind Stress
1	0.8 (2%)	0.9 (1%)	1.0 (2%)
2	2.1 (4%)	2.1 (10%)	2.5 (7%)
3	4.8 (33%)	4.2 (17%)	4.4 (12%)
4	***9.9 (51%)***	7.0 (26%)	8.2 (15%)
5	14.8 (2%)	***19.5 (34%)***	***22.3 (21%)***
6	22.0 (0%)	30.5 (7%)	Residual (3%)
7	40.0 (0%)	Residual (6%)	
8	Residual (0%)		

Table 2.7 Temporal modes of variability (days) and the respective square of the correlation (r^2) defining the variance for each of the IMFs calculated for the spring time series with the daily and multi-seasonal signal removed for surface chl-a, MLD and wind stress The dominant signal is in bold italics, the submesoscales are highlighted in green, while all modes of variability that are not significant above the 99%, are highlighted in grey.

To further investigate the relationship between possible drivers of the surface chl-a signal an EMD was carried out on both the MLD and coinciding wind stress time series (Figure 2.8). In the SAZ , the MLD has been shown to correlate well with wind stress as weak stratification in the mixed layer allows for a rapid breakdown of the mixed layer, in particular in Spring (du Plessis, 2014). The results from this study support these findings, as both the MLD and wind stress, had very similar modes of temporal variability

in spring (~2, ~4 to ~7 days for MLD and ~2, ~4 to ~8 days for wind stress, Table 2.7). These signals do appear to effect surface chl-a as similar modes of variability (~2, ~5 and ~10 days) are also dominant in the surface chl-a time series which together accounted for 88% of the surface chl-a variability. These results support the findings of Mahadevan et al. (2012) and Swart et al. (2015) whereby the mixed layer restratifies through a slumping of the lateral density gradient when the wind strength decreases. Blooms formed through eddy-driven slumping are expected to be patchier and have a greater spatial heterogeneity at submesoscales (1 to 10 km) than blooms formed from surface heating (Mahadevan et al., 2012). Therefore, if we do not sample these small scales in the SAZ we are unlikely to capture these events and would fail to accurately characterise the patchy spring blooms.

Worth noting is that both the MLD and wind stress had a dominant ~20 day signal which was not present in the surface chl-a time series. It is not clear what the driver of this temporal variability is and although worth investigating further is outside of the scope of this study.

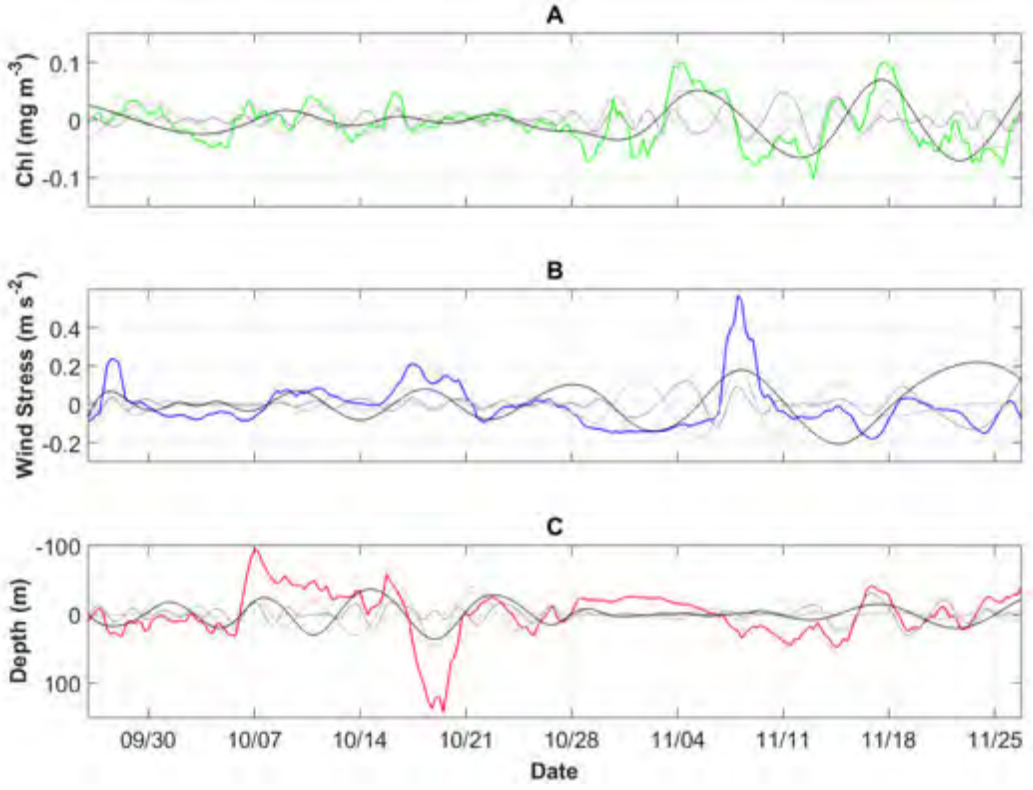

Figure 2.8 Spring time series for a) surface chl-a (green line) and ~2 day, ~5 day and ~10 day IMFs (light grey, dark grey and black lines, respectively), b) wind stress (blue line) with the ~2 day, ~4 day and ~8 day IMFs in the grey (light and dark) and black lines respectively and c) MLD (red line) with the ~2 day, ~4 day and ~7 day IMFs (light grey, dark grey and black lines, respectively).

2.4.1.2 Summer temporal variability

In summer, the combined role of solar heat flux, mesoscale features and sub-seasonal storms on the extent of the mixed layer was proposed by Swart et al. (2015) to regulate both light and iron to the upper ocean at appropriate time scales for phytoplankton growth, thereby sustaining the bloom for an extended period through to late summer. From the beginning of December until the end of the SG573 deployment (in mid-February), surface chl-a remained above 0.5 mg m^{-3}, with concentrations fluctuating (0.35 – 1.34 mg m^{-3}) at small time scales (18 hours) around a mean of 0.78 mg m^{-3}. Empirical decomposition of the summer time series showed a dominant monthly signal (~27 days) that accounted for 54% of the observed variability. The next three dominant scales of variability showed similar results to spring with three submesoscale signals (~2, ~4 and ~9 days) together describing approximately 27% of summer surface chl-a temporal variability (Table 2.8).

IMF	Surface chl-a	MLD	Wind Stress
1	0.8 (1%)	0.8 (2%)	1.0 (1%)
2	2.2 (10%)	2.3 (21%)	3.0 (32%)
3	4.2 (19%)	***6.1 (41%)***	***5.6 (45%)***
4	8.9 (6%)	13.9 (39%)	10.2 (28%)
5	***27.1 (54%)***	45.5 (8%)	19.5 (9%)
6	62.5 (0%)	Residual (0%)	38.8 (0%)
7	Residual (4%)		Residual (0%)

Table 2.8 Temporal modes of variability (days) and the respective square of the correlation (r^2) defining the variance for each of the IMFs calculated for the summer time series with the daily and multi-seasonal signal removed for surface chl-a, MLD and wind stress. The dominant signal is in bold italics, the submesoscales are highlighted in green, while all modes of variability that are not significant above the 99%, are highlighted in grey.

In summer the depth of maximum stratification shoaled from 150 m at the beginning of December to 50 m in mid-February due to an enhanced gradient in the thermocline brought on by seasonal warming of the surface waters (Swart et al., 2015). As a result, the MLD was considerably shallower in summer fluctuating +/- 16 m around a 40 m mean (Swart et al., 2015). Decomposition of the summer MLD time series showed that this variability was the result of meso- (~14 days) and submesoscale (~2 and ~6 day) signals that accounted for 39% and 54% of the variability respectively. The meso- and submesoscale signals were similar to the dominant modes of variability for summer wind stress (~3, ~6 and ~10 days) (Figure 2.9). These small scales of variability, specifically the 6 and 10 day signals, are the result of synoptic storm events that pass through the SAZ every 4 to 9 days, varying the strength of the wind stress (Braun, 2008; Swart et al., 2015). As the wind introduces periods of enhanced turbulence, which

drives a deepening of the MLD, these storms can be considered the principle driving factor of the observed meso- and submesoscale variability of the MLD in summer.

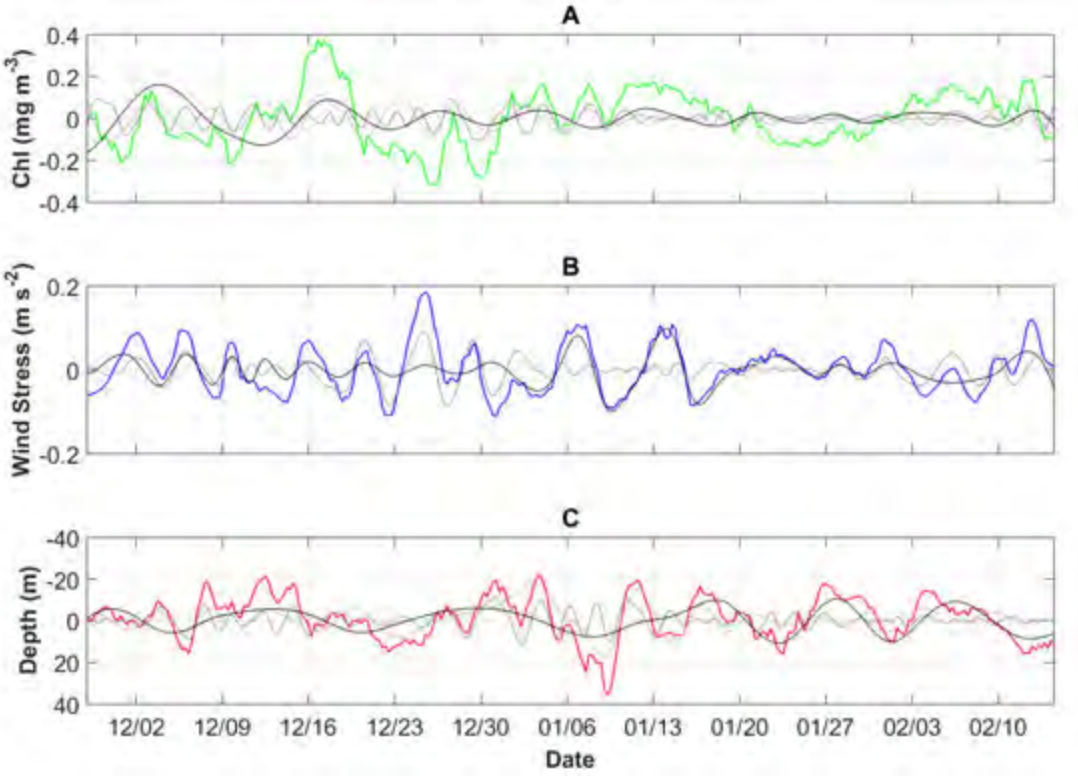

Figure 2.9 Summer time series for a) surface chl-a (green line) and ~2 day, ~4 day and ~9 day IMFs (light grey, dark grey and black lines, respectively), b) wind stress (blue line) with the ~3 day, ~6 day and ~10 day IMFs (light grey, dark grey and black lines, respectively) and c) MLD (red line) with the ~2 day and ~6 day IMFs in the grey and black lines respectively.

Although the correlation between wind stress, MLD and the surface chl-a time series was weak ($r<0.2$), EMD analysis showed that wind stress, MLD and surface chl-a variability in summer are linked. The submesoscales of variability for surface chl-a (~2, ~4 and ~9 days) were at a similar frequency as both wind stress (~3, ~6 and ~10 days) and MLD (~2 and ~6 days). These match ups in small scale temporal variability between wind stress, MLD and surface chl-a emphasise that phytoplankton variability is likely the consequence of MLD adjustments, resulting from wind stress variability occurring during synoptic scale storms in the SAZ. The low correlation between MLD and surface chl-a likely results from the variable surface chl-a to MLD adjustments in summer that causes both dilution (seen as a decrease in surface chl-a when the MLD deepens) (Crumpton and Wetzel, 1982; Banse, 1994) and growth (seen as an increase in surface chl-a in response to nutrient entrainment from a deepening MLD) (Fauchereau et al., 2011). Neither the MLD nor the wind stress has a temporal signal similar to the ~27 day period in the

summer surface chl-a time series. Again, the driver of this period of variability is unknown (although tides are a possibility) and outside the range of scales that is being studied in this thesis.

2.4.2 Sampling frequencies

Recent developments in autonomous ocean glider technology have allowed increased observations with higher resolution in both space and time (Eriksen and Perry, 2009; Mahadevan et al., 2012). From previous research, we know that if we want to sample fine scale features we need to sample at the scales of variability of the feature. However, what is unknown is the extent to which the different scales of variability count towards the overall signal that characterises the seasonal cycle (e.g. what is the minimum sampling frequency required that will allow us to adequately resolve the seasonal cycle?).

The temporal analysis EMD study found that in spring, the submesoscale (~2, ~5 and ~10 days) signals are the dominant frequencies at which surface chl-a varies. From Mahadevan et al. (2012), we know that the blooms in spring caused by eddy-driven slumping are patchy and initiate the spring bloom earlier than it would be if driven by surface heating alone. This implies that if we don't resolve the system at sub-mesoscales we will not be able to accurately characterise the seasonal cycle. In particular we are likely to incorrectly represent bloom phenology and are likely to overestimate bloom initiation dates with important implications for addressing long term trends. The temporal analysis in summer found that the variability of the sustained bloom occurred at frequencies of 2 to 9 days. Synoptic storms are proposed by Swart et al. (2015) to extend the duration of the summer bloom in the SAZ by increasing the seasonal supply of iron through MLD excursions. Therefore, if these modes of variability are not adequately sampled, it is likely that the seasonal cycle of surface chl-a will not be adequately resolved, in particular the duration of the bloom is likely to be underestimated.

Although it was not possible to investigate inaccuracies in timing or duration, by subsampling the surface chl-a spring and summer time series at the dominant frequencies, the study was able to determine to what extent we could capture the multi-seasonal mean and standard deviation of the original high-resolution time series.

Subsampling at the dominant set frequencies for both spring and summer captured the multi-seasonal means. However, the randomly extracted samples also captured the mean (Table 2.9). In spite of this, capturing the mean does not characterise the multi-seasonal cycle of surface chl-a variability. Comparison of the standard deviation found that the set frequency samples on average had a standard

deviation that was similar to the original high resolution time series, while the randomly extracted standard deviations were highly variable (see Figure 2.6). Therefore, sampling at the dominant scales of variability and at a set frequency in both spring and summer captures the multi-seasonal variability around the mean better than that of random extractions (Table 2.9). RMSE analysis of the standard deviation further emphasises this as there is a greater chance of incorrectly predicting surface chl-a variability if surface chl-a is randomly sampled (Figure 2.10). The exception to this is the 27 day set frequency in summer that does worse at correctly predicting surface chl-a variability than the equivalent random extractions.

Season	Sampling day	Mean	Standard deviation
Spring	Time series	0.38	0.12
	5 day subsampling	0.38	0.12
	5 day random	0.39	0.12
	10 day subsampling	0.39	0.13
	10 day random	0.39	0.12
Summer	Time series	0.78	0.14
	4 day subsampling	0.78	0.14
	4 day random	0.76	0.13
	9 day subsampling	0.78	0.15
	9 day random	0.79	0.14
	27 day subsampling	0.73	0.06
	27 day random	0.76	0.13

Table 2.9 The average mean and standard deviations for the time series, subsamples and random extractions for both spring and summer.

From RMSE analyses (difference between values predicted by an estimator and values actually observed), the study was also able to determine the minimum frequency needed to accurately characterise the mean and standard deviation of the spring and summer surface chl-a time series. Subsampling at periods of 10 days or less will ensure that meso- and submesoscale variability of phytoplankton in the SAZ during spring will be captured (Figure 2.10 a). Similarly, in summer, subsampling at higher frequencies (less than 10 days) is required to capture the meso- and submesoscale forcing that drives the short term variability observed in surface chl-a (Figure 2.10 b). Sampling at larger temporal frequencies would capture the overall multi-seasonal trend of an increase in surface chl-a from spring to summer but not the sub-seasonal meso- and submesoscale variability observed in surface chl-a. Therefore, to adequately resolve and characterise the seasonal scales of

variability of phytoplankton in the SAZ, surface chl-a needs to be subsampled at set frequencies (less than 10 days) in both spring and in summer to resolve for the required scales of variability.

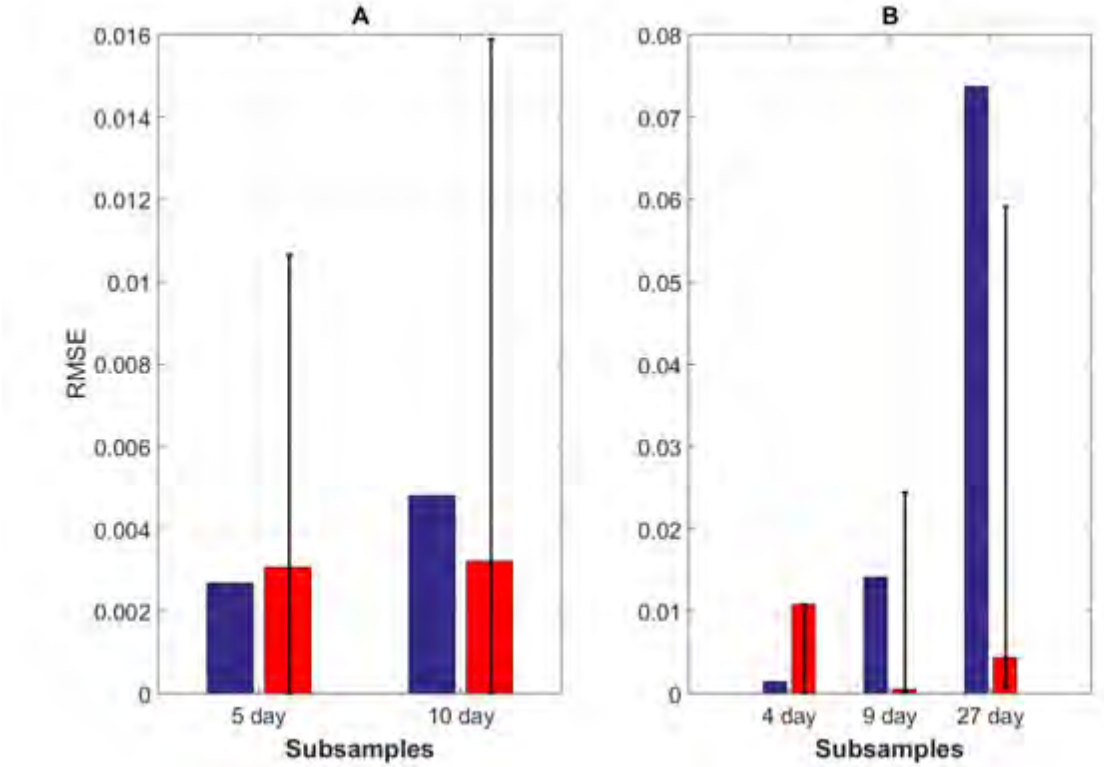

Figure 2.10 The root mean square error of standard deviation for subsampling at the dominant frequencies (blue) and at random (red) for (A) spring and (B) summer surface chl-a. The range of possible errors of randomly sampling at each frequency is shown with the black line.

Models, therefore need to parameterise for these small scales of variability, in order to adequately represent the drivers of the seasonal characteristics of phytoplankton in the SAZ, over and above the multi-seasonal ramp. Hence, observation platforms (e.g. Argo floats, gliders) need to collect data at smaller scales (less than 10 days) to adequately resolve for these drivers of the phytoplankton seasonal cycle in the SAZ.

2.5 Conclusion

In the SAZ, the multi-seasonal signal is the dominant source of surface chl-a variability over the 5.5 month period of the glider deployment, explaining 58% of the temporal variability of surface chl-a. Additionally a dominant daily signal in surface chl-a was observed (20 hours at 7% and 9% for multi-seasonal and spring, respectively and 18 hours at 22% for summer). The removal of both the daily and multi-seasonal signal allowed for the observation of the sub-seasonal signals. The meso- and submesoscale signals explained the majority of the surface chl-a variability for the full multi-seasonal time series (53%) as well as when separated into spring (97%) and summer (27%).

An investigation of the spring versus summer analysis showed that the magnitude of phytoplankton variability was similar in spring and summer, with surface chl-a variability occurring at submesoscales. In spring, the submesoscale (~2, ~5 and ~10 day) signals were the only significant temporal signals (above 99% confidence level) and combined they explain 97% of the temporal variability of surface chl-a. In summer the dominant mode of variability was a monthly (~27 day) signal, however submesoscale signals (~2, ~4 and ~9 day), described approximately 27% of the remaining surface chl-a temporal variability. Although these surface chl-a signals have similar scales of inter-seasonal variability, the drivers of the variability differ.

In spring both the MLD and wind stress have a dominant ~20 day signal that is not present in surface chl-a, however their submesoscale modes of temporal variability (~2, ~4 to ~7 days for MLD and ~2, ~4 to ~8 days for wind stress) are similar to those of the surface chl-a (~2, ~5 and ~10 days) and dominate the remaining variability of the MLD and wind stress. The relationship between surface chl-a, MLD and wind stress can be explained by Mahadevan et al. (2012) and Swart et al. (2015), where the patchy surface chl-a blooms are formed through the slumping of the lateral density gradient when the wind stress weakens and eddies restratify the mixed layer at submesoscales (~2 to ~7 days), before the occurrence of surface heating stratification. During summer, the MLD was dominated by meso- (~14 days) and submesoscales (~2 and ~6 day) of temporal variability, while wind stress similarly varied at submesoscales (~3, ~6 and ~10 days). The submesoscales of variability for surface chl-a (~2, ~4 and ~9 days) were at a similar frequency as both wind stress and MLD. These match ups in small scale temporal variability between wind stress, MLD and surface chl-a are the consequence of MLD adjustments, resulting from wind variability occurring during synoptic scale storms in the SAZ.

Subsampling at the dominant set frequencies and at random extractions for both spring and summer captured the multi-seasonal means. However, capturing the mean does not characterise the seasonal cycle of surface chl-a variability. Comparison of the standard deviation found that the set frequency samples on average had a similar standard deviation to the multi-seasonal time series, while the randomly extracted standard deviations were highly variable. Therefore, sampling at a set frequency in both spring and summer captures the multi-seasonal variability around the mean better than that of random extractions. Through RMSE analyses, the study was able to determine that to adequately resolve and characterise the sub-seasonal scales of variability of phytoplankton in the SAZ, surface chl-a needs to be subsampled at set frequencies (less than 10 days) in both spring and in summer.

Chapter 3:

Quantifying the spatial scales of phytoplankton variability in the Sub-Antarctic Southern Ocean using high-resolution satellite and glider datasets

3.1 Introduction

Over the years, spatial heterogeneity of phytoplankton has regularly been observed in satellite ocean colour images. Similar to temporal variability, phytoplankton spatial variability is thought to be driven by a combination of physical and biological processes.

Phytoplankton are passive particles. As such, ocean physics has a strong effect on their spatial distribution. Eddies, fronts and filaments induce stirring and mixing of the upper ocean which alters the properties of the surface layer of the ocean. The advection of upper ocean properties is dominated by horizontal velocities, which affects the distribution of phytoplankton (Mahadevan, 2016). In addition, vertical motion in the upper surface layer also affects phytoplankton distribution through modulating the gradients of light and nutrients. Submesoscale processes induce vertical transport of both nutrients and phytoplankton up and down the water column (Mahadevan, 2016). This impacts the growth of phytoplankton by controlling their access to light and nutrients. Phytoplankton spatial variability is also affected by non-linear biological processes such as zooplankton grazing (Martin, 2003). Other processes such as phytoplankton growth and mortality depend on changes to the availability of local nutrients and light, which is affected by local physics and external factors. All these biological and physical processes contribute to the complex spatial variability observed in phytoplankton distributions.

Phytoplankton in the Southern Ocean are highly variable in space. The Sub-Antarctic Zone (SAZ) in particular, has been characterised as having intermittent and patchy phytoplankton blooms in spring, while in summer, blooms that are still intermittent but large, homogenous and sustained throughout summer (Swart et al., 2015). Understanding the different inter-seasonal scales of spatial variability of chlorophyll (chl-a) is important for determining the extent that primary production impacts the global carbon cycle. Satellites are currently the most effective way in which to monitor the spatial variability of surface chl-a (Reilly et al., 1998; Marrari et al., 2006). Through the use of daily high-resolution (2 km) ocean colour satellite data, seasonal and sub-seasonal phytoplankton variability in the SAZ can be investigated.

Key Questions

This study uses surface chl-a data collected from both a high-resolution (6 hourly profiles) glider transect in the SAZ together with high-resolution satellite ocean colour data (daily, 2 km resolution) to investigate the spatial variability of phytoplankton in spring and summer in the SAZ. Satellites provide a

novel way to assess phytoplankton spatial variability over large areas and will help in answering the following questions.

1. How does the observed spatial variation in surface chl-a change with length scales in the SAZ?

Spatial heterogeneity of phytoplankton is one of the oldest oceanographic observations, where phytoplankton spatial distributions can range from meters to basin scale. Phytoplankton heterogeneity is formed by the variable response of phytoplankton to physical properties (e.g. meso- and submesoscale eddies, fronts and filaments) and the availability of light and nutrients in the euphotic zone. However, very little research has been done on phytoplankton spatial variability in the Southern Ocean. By comparing the spatial variance of surface chl-a and sea surface temperature (SST) satellite images as a function of the size of a region at different length scales, we can begin to understand the spatial variability of phytoplankton in the SAZ.

2. Does the magnitude of phytoplankton spatial variability change seasonally?

Phytoplankton in the SAZ is known for having high inter-annual and intra-seasonal variability. A study by Swart et al. (2015) found that sub- and mesoscale features cause chl-a blooms to be intermittent and patchy in spring whereas in summer the chl-a bloom is more homogenous in space. This question aims to identify the multi-seasonal variability of phytoplankton distribution through characterising the spatial variance of chl-a as a function of the size of a region at various scales for both spring and summer satellite ocean colour images.

3. To what extent is the variability that gliders measure due to spatial patchiness?

The development of gliders has become useful in collecting data at high spatial and temporal resolution for long periods of time allowing a detailed assessment of chl-a variability. Nevertheless, issues about the quasi-Lagrangian nature of gliders and the possible confusion of temporal and spatial variability have been raised. Analysis of chl-a spatial variability of satellite data from consecutive days with the variability of surface chl-a data from gliders can be performed to determine the extent to which spatial patchiness is causing surface chl-a variability in glider observations.

3.2 Data and methods

3.2.1 Satellite products

3.2.1.1 Ocean colour

Ocean colour data was obtained from MODIS-Aqua (Moderate-resolution Imaging Spectroradiometer) for analysis of chl-a distribution. MODIS is an instrument on board the NASA Aqua satellite. Aqua orbits around the earth at 705 km on a circular, sun-synchronous, near-polar ascending node (13:30). MODIS-Aqua views the entire globe every 1 to 2 days in 36 spectral bands. Ocean colour is observed between bands 8-16 with wavelengths between 405-536 nm (Franz et al., 2005). The MODIS-Aqua chl-a algorithm returns near-surface chl-a concentrations. These concentrations are calculated using an empirical relationship derived from *in situ* measurements of chl-a (*chloro_a*) for MODIS-Aqua ocean colour) and blue to green band ratios of *in situ* remote sensing reflectance (Rrs). The Rrs occurs at 2-4 wavelengths between 440-570 nm. The algorithm used is a 4th order polynomial relationship between a ratio of Rrs and *chloro_a*.

$$log_{10}(chloro\_a) = a_0 + \sum_{i=1}^{4} a_i log_{10}\left(\frac{R_{rs}(\lambda_{blue})}{R_{rs}(\lambda_{green})}\right)^i \Big|, \quad (3.1)$$

Level-2, daily, 1 km resolution data was obtained from the NASA Ocean Color website (http://oceancolor.gsfc.nasa.gov/cgi/browse.pl?sen=am). The daily swaths covered the area (40°S to 45°S and 12°W to 0°) of the SG573 track during the deployment of the glider. Ocean colour data were retrieved for one year between June 2012 and May 2013. The level-2 data were further processed in SeaDAS (SeaWiFS Data Analysis System), an image analysis package for processing, displaying and analysing satellite ocean colour data (http://seadas.gsfc.nasa.gov/). In SeaDAS, the data were binned into level-3 data and generated into level-3 mapped (platecarree) data at 2 km resolution. The 2 km resolution data were generated from the 1 km data in order to remove any outliers that occurred in the 1 km data.

The days with the most number of ocean colour data points (over 30 000) within the period of glider deployment were found (11 days in total). Of these days, only 7 days had ocean colour data that coincided with the glider track for that day. The 7 days were the 5th, 7th and 15th of October 2012, 27th November 2012, 9th December 2012, 23rd and 27th of January 2013 and 2nd February 2013.

3.2.1.2 Sea surface temperature

Satellite sea surface temperature was obtained from MODIS Aqua (http://oceancolor.gsfc.nasa.gov/cms/). The SST data used was daily, level-3 mapped data at a 4km resolution. MODIS wave bands 31 and 32 were used at 11 and 12 µm. Daily SST satellite data was taken for the same days as the 2 km ocean colour satellite data. For the 15 October 2012 and 23 January 2013, there was no SST data for the area. Instead, SST data from 26, 29 and 30 January 2013 were used for the 23 January. No SST satellite data that covered the research area a week before or after was found on 15 October 2012.

3.2.2 Spatial analysis

Spatial heterogeneity was characterised using a similar approach to that used by Mahadevan and Campbell (2002), where the spatial variance V is determined in terms of various length scales, L. Standard deviation S was used instead of variance for this analysis. The standard deviation was calculated over an area of dimension L (5° by 5°; Figure 3.1), and then over subdomains of dimension $L_i=L/2^i$ ($i = 0, 1, 2, 3, \ldots, N$) ($L/2, L/4, L/8\ldots$), into which the region was partitioned. $S(L_i)$ is then the average standard deviation contained within all subdomains of area L_i^2 that covers the domain. The standard deviation for each day was normalised by the total standard deviation of the largest domain.

This analysis of spatial variance in terms of length scales assumes the existence of a scaling relationship between variance and the spatial scales. The underlying theoretical concept is that standard deviation varies more or less linearly with length scales in a logarithmic space. This suggests that there is a power law relationship in the form of:

$$S \sim L^p \tag{3.2}$$

Where p>0 and is the slope parameter. This power law relationship characterises the standard deviation as a function of the size of a region. The slope p is a measure of the spatial heterogeneity of the distribution of the property. The variations in p reflect differences in the total standard deviation retained at small scales. Therefore, the log(S) vs log(L) plots whose standard deviation $S(L)$ have smaller slopes (p), have a greater variance contained in small scales and have a patchier distribution than one that has a larger slope (Mahadevan and Campbell, 2002).

The spatial variance was calculated for both the satellite ocean colour and SST images (Table 3.1) and the data were normalised to allow comparison between the variables. The normalised data sets were divided into spring and summer, to assess the inter-seasonal (whether the relation for each variable changes with the season) and inter-variable (how chl-a and SST vary from each other in one season) spatial variability. It is not possible to do any statistical testing on the difference between spring and summer spatial variability as there are not enough days with sufficient data.

Date	Chl-a Longitude	SST Longitude	Glider co-ordinates
5 October 2012	7° to 12° W	7° to 12° W	-42.8° S and -9.6° W
6 October 2012	7° to 12° W	7° to 12° W	-42.9° S and -9.5° W
15 October 2012	7° to 12° W		-42.9° S and -8.9° W
27 November 2012	7° to 12° W	7° to 12° W	-41.8° S and -6.4° W
9 December 2012	2° to 7° W	7° to 12° W	-41.6° S and -5.8° W
23 January 2013	0° to 5° W		-42.8° S and -3.5° W
26 January 2013		7° to 12° W	-42.8° S and -3.2° W
29 January 2013		1° to 6° W	-42.8° S and -3.0° W
30 January 2013		1° to 6° W	-42.7° S and -3.0° W
2 February 2013	1° to 6° W	7° to 12° W	-42.5° S and -3.0° W

Table 3.1 Longitudinal values for the chl-a and SST 5° by 5° images. All the latitudes where from 40° to 45° S. Glider co-ordinates at midday for that specific day.

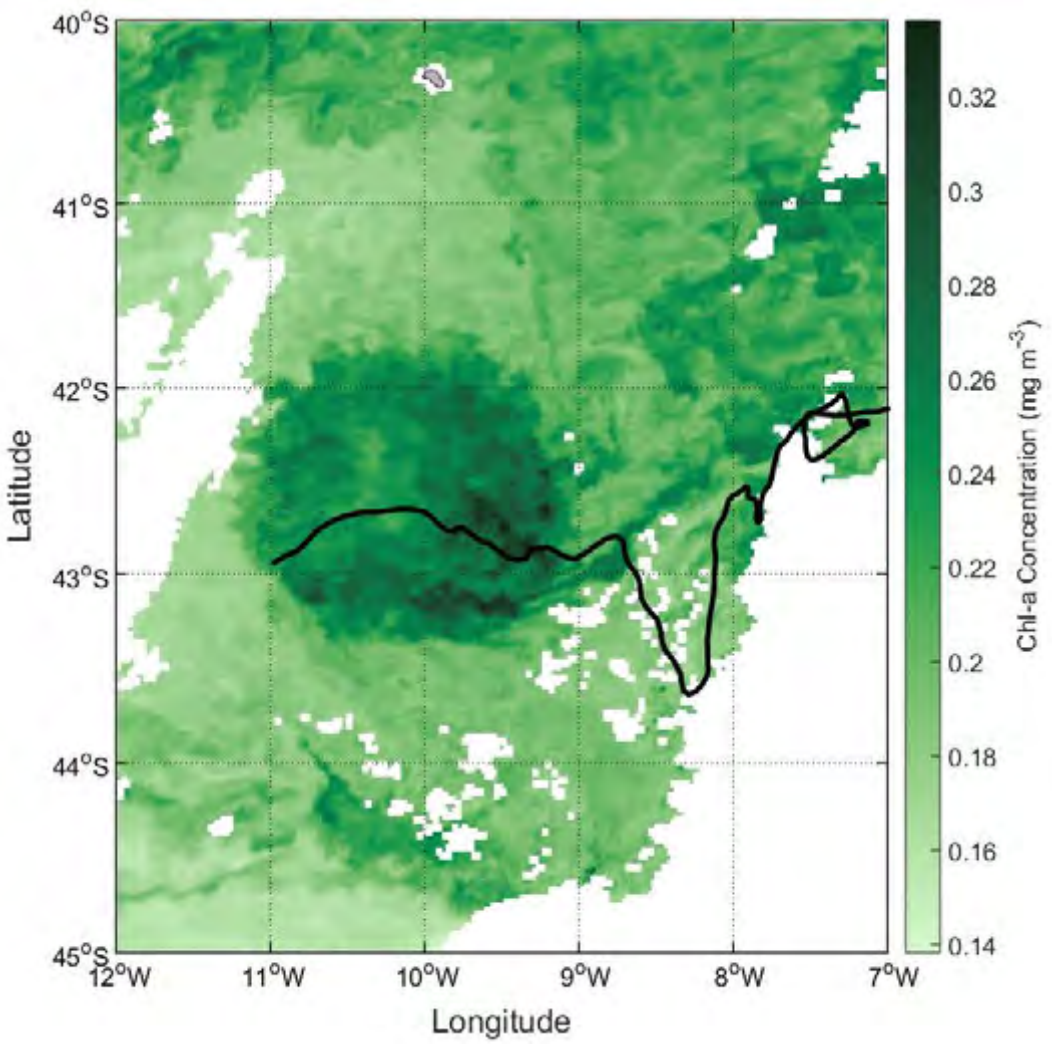

Figure 3.1 MODIS Aqua satellite ocean colour image for the 6 October 2012 at 2 km resolution in the 5° by 5° grid (L) used for spatial analysis. The glider track is in black.

3.3 Results

3.3.1 Chl-a spatial variability

Seven days of satellite ocean colour data were found to coincide with the positions of the glider. Of these days, three occurred in spring (5, 6 and 15 of October 2012), one occurred over the transition phases between spring and summer (27 November 2012) that Swart et al. (2015) proposed. The remaining three days (9 December 2012, 23 January and 2 February 2013) occurred in summer.

The spatial analysis performed on all of the days showed that the relationship between standard deviation and length scales was logarithmic, as expected, and that the standard deviation decreases at smaller scales. There also appears to be a greater range in standard deviation from large to small length scales in summer (mean standard deviation range = 0.21) than in spring (mean standard deviation range = 0.04). The transition phase (27 November 2012) chl-a standard deviation followed a similar trend as the summer chl-a standard deviation data. From henceforth the 27 November chl-a data will be associated with the summer chl-a images (Figure 3.2).

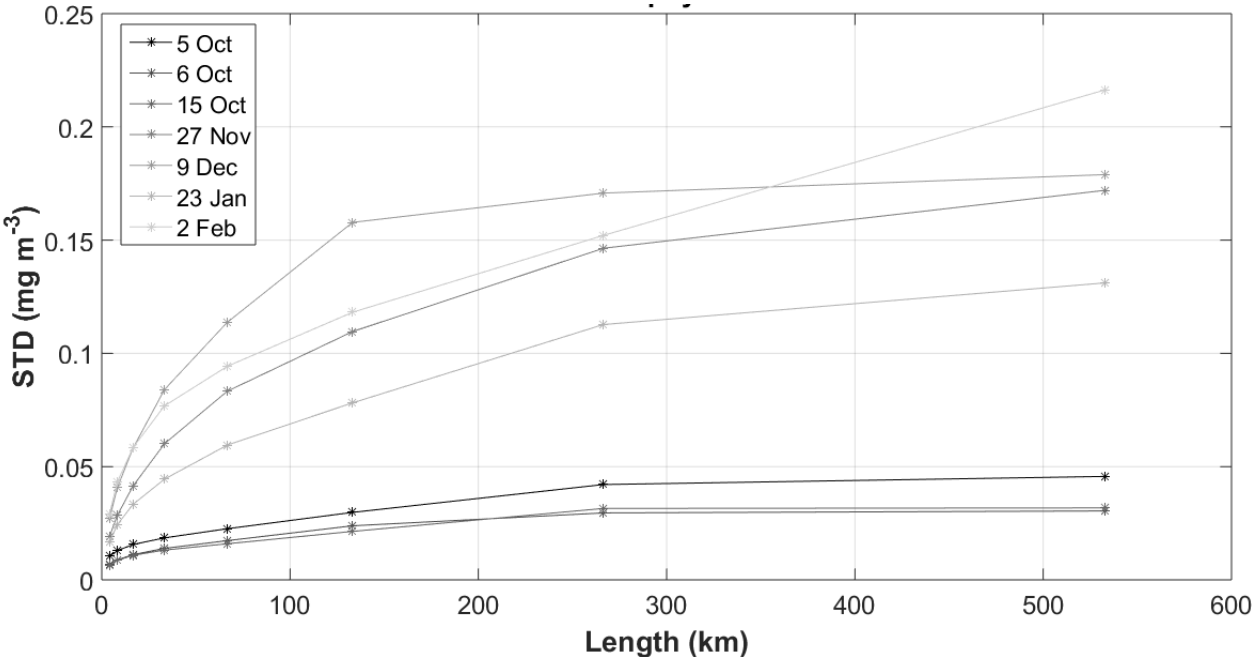

Figure 3.2 Spatial standard deviation of chl-a at eight length scales (4 to 533 km).

The parameters of the power law were estimated with a log-log regression. For both spring and summer, the parameter of the slopes is relatively low (Table 3.2) with a difference of 0.14. However, the slope parameters in summer (mean p = 0.42) were slightly steeper than in spring (mean p = 0.33).

Date	p
5 October 2012	0.32
6 October 2012	0.33
15 October 2012	0.34
27 November 2012	0.46
9 December 2012	0.41
23 January 2013	0.43
2 February 2013	0.39

Table 3.2 Slope parameter (p) for the logarithmic function of chl-a between standard deviation and length scales (Equation 3.2).

3.3.2 SST spatial variability

Satellite SST data sets were obtained for all the same days as chl-a, except for the 15 October 2012 and 23 January 2013. Three substitute days were found for 23 January 2013 – 26, 29 and 30 January 2013. Spatial analysis of the SST found that the standard deviation from large to small length scales ranged between 2.18 to 0.11 (Figure 3.3).

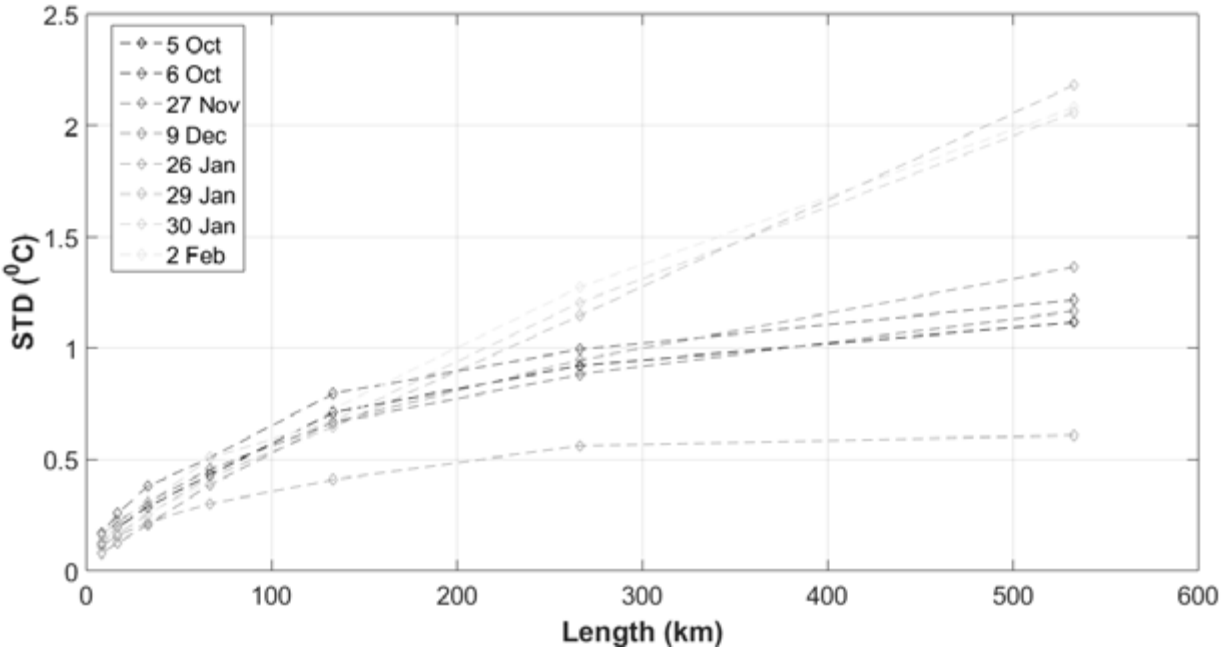

Figure 3.3 Spatial standard deviation of SST at seven length scales (8 to 533 km).

Further analysis through the power law relationship found that there was very little difference between the inter-seasonal slope parameters (Table 3.3). The summer slope parameters (mean p = 0.67) were slightly steeper than in spring (mean p = 0.56). The exception to this was the 26 January 2013, were the slope parameter was relatively low (p = 0.42) in comparison to the rest of the SST data. Contrasting to

chl-a spatial analysis, the 27 of November followed a similar slope trend as the SST spring standard deviation data.

Date	P
5 October 2012	0.55
6 October 2012	0.48
27 November 2012	0.49
9 December 2012	0.71
26 January 2013	0.42
29 January 2013	0.71
30 January 2013	0.61
2 February 2013	0.68

Table 3.3 Slope parameter (p) for the logarithmic function of SST between standard deviation and length scales (Equation 3.2).

3.3.3 Intra-variable analysis

In order to compare chl-a spatial variability to that of SST, the spatial standard deviation for each day was normalised by the total standard deviation of the largest domain (*L*) and the power law parameter recomputed (Table 3.4). Overall, the chl-a slope parameter (mean p = 0.40) was smaller than SST (mean p = 0.59), while the standard deviation for chl-a was higher than SST at all length scales. This, implies that chl-a maintains a larger spatial variability than SST at small scales, indicating that chl-a is patchier than SST (Table 3.4).

Date	Chl-a P	SST P
5 October 2012	0.32	0.59
6 October 2012	0.35	0.52
15 October 2012	0.36	
27 November 2012	0.49	0.50
9 December 2012	0.46	0.74
23 January 2013	0.44	
26 January 2013		0.45
29 January 2013		0.68
30 January 2013		0.58
2 February 2013	0.38	0.65

Table 3.4 Slope parameter (p) for the normalised logarithmic function of chl-a and SST standard deviation (Equation 3.2).

During spring there are two distinctly different slopes between chl-a and SST. Chl-a standard deviation was higher than SST spring standard deviation for all length scales. The average slope for chl-a (mean p = 0.34) was lower than SST (mean p = 0.54), indicating that in spring chl-a is patchier than SST. In summer,

chl-a and SST spatial analysis found that the slopes were more similar. This is mostly because SST has larger variation in the parameter from day to day. Although the slopes are similar, chl-a is flatter (mean p = 0.44) in comparison to SST (mean p = 0.60), with the exception of 27 November 2012 (p = 0.50) and 26 January 2013 (p = 0.45), where the slopes are similar to that of summer chl-a. The spatial variability for the 9 December 2012 (p= 0.74) does not follow the same trend as either summer SST or chl-a data.

3.4 Discussion

The heterogeneity of phytoplankton spatial distribution arises from a combination of biological and physical process at meso- and submesoscales (Van Gennip et al., 2016). Mahadevan and Campbell (2002) proposed a way to characterise the spatial variance of properties as a function of spatial scales. In the SAZ, phytoplankton is known for being patchy in spring whereas in summer phytoplankton blooms are thought to be more homogenous in space (Swart et al., 2015). Although studies have found this to occur, the extent to which this spatial variability of phytoplankton occurs is relatively unknown.

3.4.1 Chl-a and SST spatial analysis

Spatial analysis of the chl-a images using Mahadevan and Campbell's (2002) power law indicates that similar spatial variability of chl-a occurs in spring and summer (Figure 3.4). Both the power law exponents, p, for spring and summer are relatively small ($p = 0.33$ and 0.42) and suggest that phytoplankton is patchy across all length scales, as a smaller exponent infers greater patchiness. These results are similar to those of Mahadevan and Campbell (2002) who ran a spatial analysis study in the North Atlantic.

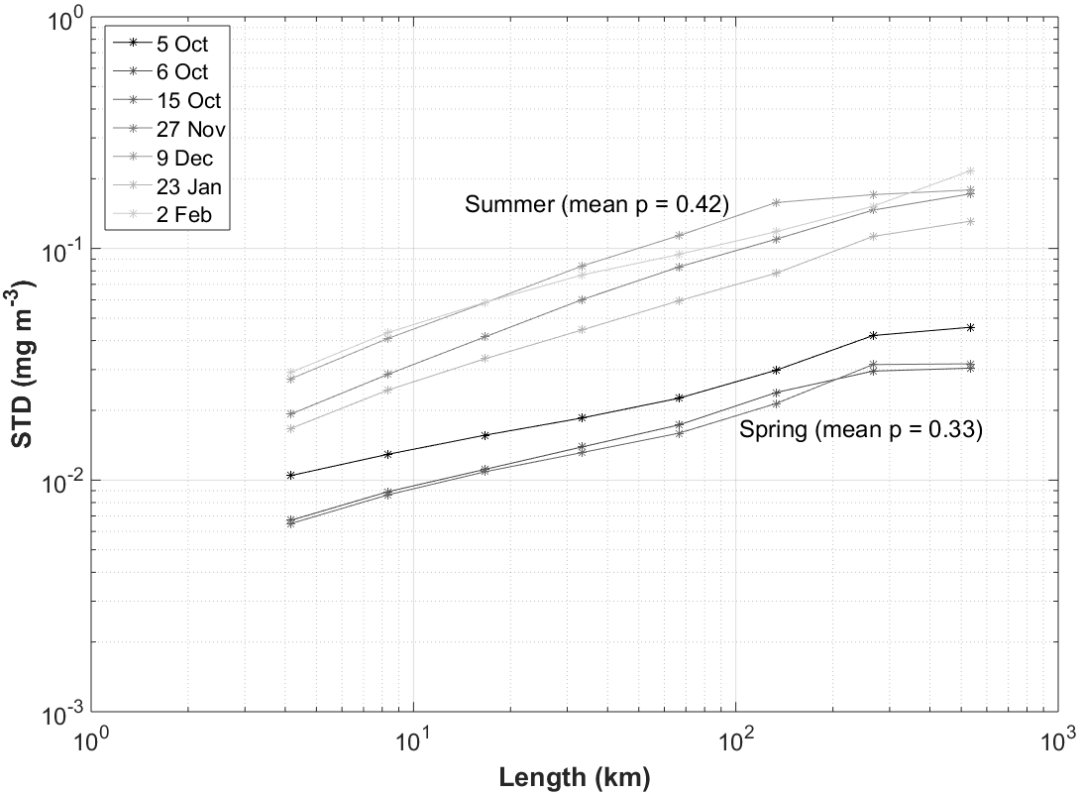

Figure 3.4 The log(S) vs log(L) curves from the 7 chl-a images found in the SAZ for the period of glider deployment. The length scales analysed ranged from 2 to 533 km. The slopes indicated are estimated for lines fitted to the points between L = 4 km and 533 km (see Table 3.4).

Although there is very little difference in inter-seasonal patchiness of chl-a, there is an inter-seasonal difference in standard deviation between spring and summer chl-a concentrations. During summer both the mean and maximum chl-a concentration is higher than during spring. The spatial analysis found that the variation around the mean in summer is also higher (as much as two orders of magnitude) compared to spring. These higher chl-a variations could be a result of different underlying inter-seasonal physics and/or greater phytoplankton growth in summer.

SST was used as a proxy for understanding the variability in upper ocean physics, in order to find out if physical patchiness was connected to the observed chl-a patchiness. Inter-seasonal comparisons of SST found that there was very little difference between spring and summer variability in upper ocean physics (difference in p = 0.1) (Figure 3.5). This suggests that patchiness in upper ocean physics in spring and summer is similar at all length scales (p = 0.56 and 0.67). Unlike chl-a, there is relatively no inter-seasonal difference between spring and summer SST standard deviation around the multi-seasonal means.

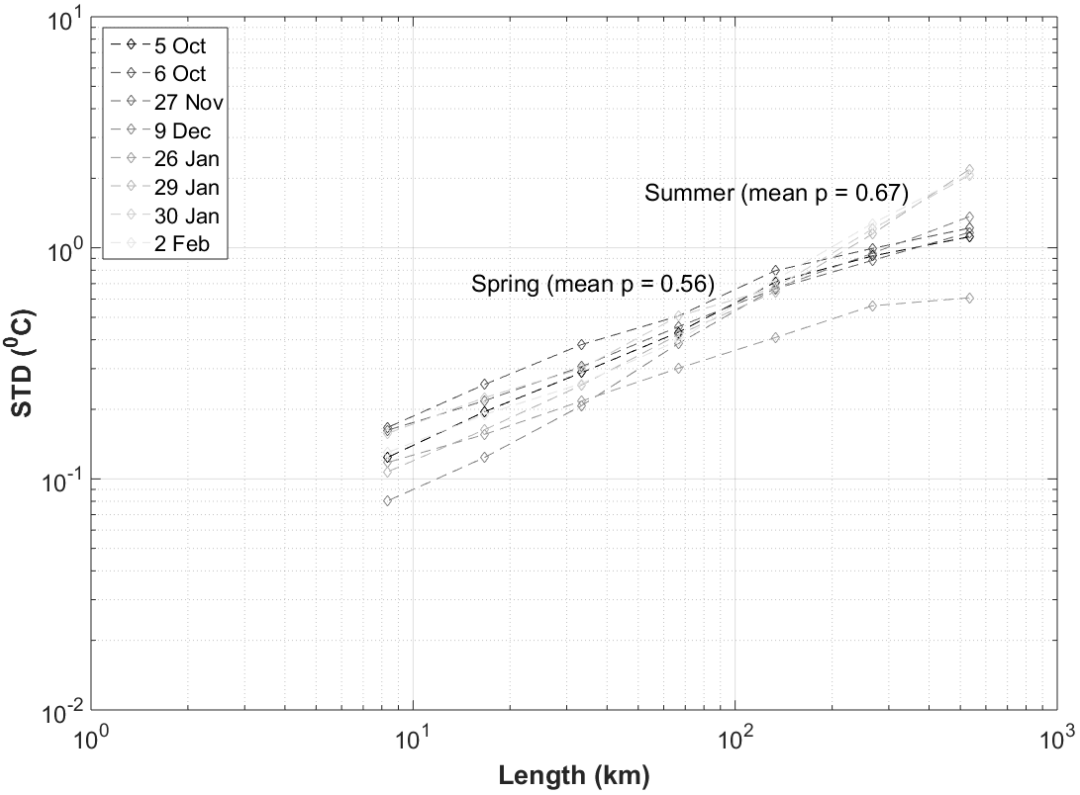

Figure 3.5 The log(S) vs log(L) curves of 8 SST images in the SAZ for the period of glider deployment. The length scales analysed ranged from 4 to 533 km. The slopes indicated are estimated for lines fitted to the points between L = 8 km and 533 km (see Table 3.4).

3.4.2 Inter-variable comparison

Spatial analysis found that chl-a in summer is less patchy than in spring, but that there is a higher variance in chl-a in summer. From various studies we know that in the Southern Ocean there is a greater response in phytoplankton to growth during summer than in spring due to increased light availability (Boyd, 2002; Arrigo et al., 2008). However, phytoplankton in summer become nutrient (iron) limited. Through the use of SST as a proxy for physics, we know that the patchiness of physics is similar in spring and summer. Although, the patchiness of physics is similar inter-seasonally, the important effects on the environment (from a biological point of view) are different. In spring small scale physics improves the light regime through enhanced stratification whereas in summer the physics enhances mixing which elevates nutrient concentrations in the euphotic zone. This elevation in nutrients along with sufficient light in summer allows for greater growth to occur in summer than in spring which is typically light limited. Maximum chl-a concentrations in spring are thus low and as such the amplitude of the standard deviation is limited, whereas in summer, maximum chl-a concentrations are high allowing a greater

degree of variability to occur. Therefore, it can be argued that this growth term in summer is creating the offset between higher chl-a variance in summer than in spring.

In the ocean, the response time of SST to heat flux is usually much longer than the time scales of biological uptake (Mahadevan & Campbell, 2002). This typically explains why biological variables such as sea surface chl-a, are spatially patchier than SST at mesoscales, as observed in the North Atlantic by Mahadevan and Campbell (2002). The results derived from the comparison between the normalised slopes of the log-log *S(L)* curves of SST and chl-a (Figure 3.6) show that the power law exponents of the SST (mean p = 0.59) were on average greater than those for chl-a (mean p = 0.40). This verifies that chl-a is patchier than SST over the range of length scales analysed. These results also confirm what Mahadevan and Campbell (2002) observed in the North Atlantic, where chl-a had greater variance at small length scales than SST.

Seasonally, there is larger patchiness in phytoplankton in spring compared to summer. This is because on average there is a greater difference between spring chl-a and SST power law exponents (mean difference of p = 0.2) (Figure 3.6 a) than in summer (mean difference of p = 0.16) (Figure 3.6 b). This difference in seasonal patchiness, confirms what Swart et al. (2015) suggested in their study with gliders, that phytoplankton blooms in spring are patchy, whereas in summer the phytoplankton blooms appeared to be more homogenous due to their forcing by synoptic storms. Although there is a small reduction in chl-a patchiness during summer time compared to spring (Figure 3.4), the spatial variability of some of the SST days (27 November 2012 and 26 January 2013) is more similar to chl-a spatial variability than SST (Figure 3.6 b). The similarity between the spatial variability during these days may be due to the passage of storms which might contribute to chl-a patchiness. However, this hypothesis cannot be tested due to the lack of data in the area during storms.

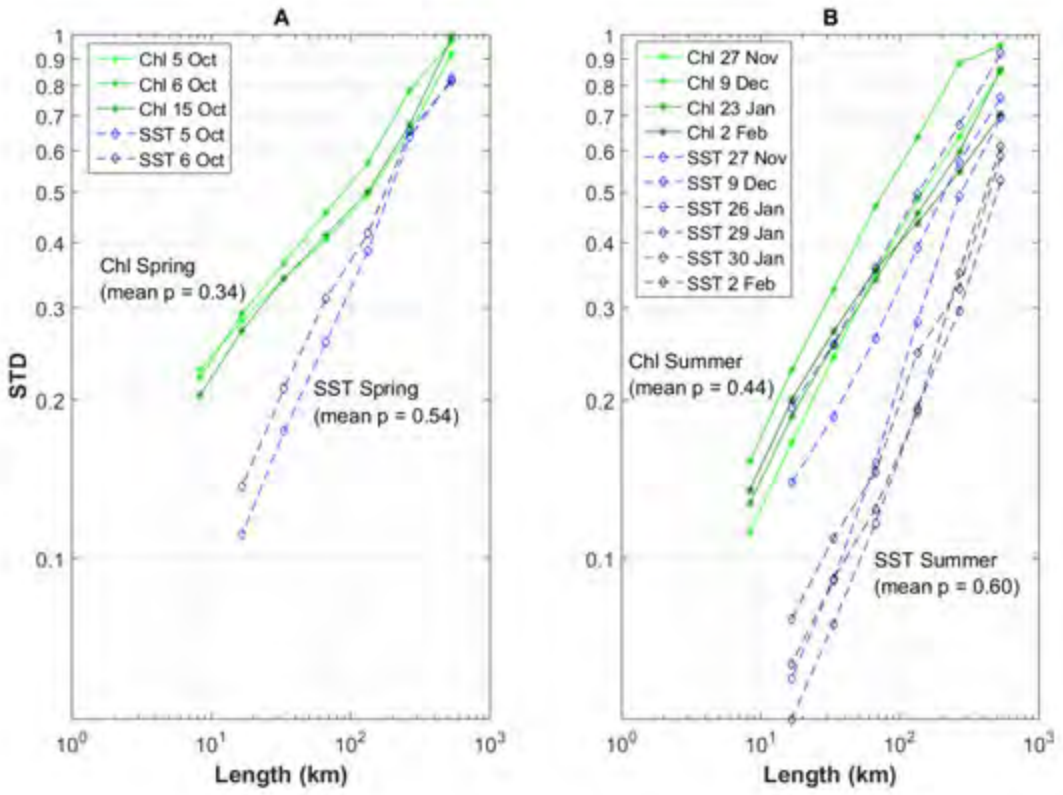

Figure 3.6 The normalised log(S) vs log(L) curves for A) spring and B) summer chl-a and SST images in the SAZ for the period of the glider deployment. Chl-a curves are the solid green lines and SST curves are the dashed blue lines.

Mahadevan and Campbell (2002) spatial analysis in the North Atlantic, also characterised spatial heterogeneity of chl-a as patchier than SST at small scales, which is similar to the results of this study. A comparison of Mahadevan and Campbell (2002)'s chl-a spatial analysis in the North Atlantic to this study in the SAZ found that the slope parameters in the North Atlantic were smaller (Table 3.5) than in the SAZ (Table 3.6). This suggests that chl-a in the North Atlantic is more spatially patchier than in the SAZ. However, understanding the possible drivers of this difference in patchiness is not possible as the specific period nor location of their study is not known and therefore cannot directly compare the two spatial analysis.

Date	Chl-a P	SST P
M-336	0.1	0.6
S/A-278	0.1	0.52
S/A-286	0.1	0.58
S/A-288	0.1	0.52

Table 3.5 Mahadevan and Campbell (2002) slope parameter (p) for the normalised logarithmic function for variance in chl-a and SST in the North Atlantic.

Date	Chl-a P	SST P
5 October 2012	0.64	1.18
6 October 2012	0.71	1.04
15 October 2012	0.72	
27 November 2012	0.98	1.01
9 December 2012	0.91	1.49
23 January 2013	0.89	
26 January 2013		0.91
29 January 2013		1.36
30 January 2013		1.15
2 February 2013	0.77	1.31

Table 3.6 Slope parameter (p) for the normalised logarithmic function for variance in chl-a and SST in the SAZ.

3.4.3 Spatiotemporal analysis of satellite and glider data

Since the development of gliders, their quasi-Lagrangian nature of sampling ocean properties in space and time has been questioned. In recent years, it has been suggested that chl-a variability and patchiness is a result of gliders moving into different water masses and inducing patchiness as opposed to temporal adjustments in phytoplankton biomass (e.g. growth or loss). The spatial analysis performed on the satellite data in the previous section (see Section 3.4.1 and 3.4.2) was able to remove any element of geography that would affect spatial variability of the phytoplankton. The results, therefore are purely about variance at different spatial scales. By finding consecutive days of satellite images within a 10 day period a temporal component was added to the study and compare the satellite spatial variance to glider data, to determine the extent to which spatial patchiness is causing surface chl-a variability in glider observations.

3.4.3.1 Statistical analysis of spatiotemporal variability

The standard deviation was calculated for satellite and glider surface chl-a for a period less than 10 days as sampling surface chl-a at a period more than 10 days reduces the ability to capture phytoplankton multi-seasonal and sub-seasonal variability (see Section 2.4.2). Spatial distance less than 100 km was used to avoid capturing variability from different water masses. Only the spatial-temporal variability in spring was analysed, as of the seven days that had sufficient satellite chl-a data, only three days in spring were within a 10 day period of each other. A 6 day temporal period was chosen for the glider as it fell half way between the dominant ~2, ~5 and ~10 day temporal periods found in spring (see Section

2.4.1.2). For the glider surface chl-a spring time series, the standard deviation was calculated for randomly subsampled 6 day periods. This standard deviation was compared to the standard deviation from the spatial analysis of satellite data at 66.6 km (*L/8*) as this was the closest length scale that matched the glider's average distance (76.2 km) travelled in 6 days in spring.

3.4.3.2 Spatiotemporal comparison of the satellite and glider data

The mean standard deviation from the spatial analysis at 66 km for the satellite chl-a data was 0.019, which was one third of the mean standard deviation calculated for the 6 day glider periods (mean standard deviation = 0.060, Table 3.7). Similarly, the difference in the daily satellite standard deviation (range = 0.0066) was smaller than the 6 day glider periods (range= 0.086).

Date	Standard deviation
5 October 2012	0.022
6 October 2012	0.017
15 October 2012	0.016
Glider 6 day period	0.060

Table 3.7 Slope parameter (p) for the normalised logarithmic function for variance in *surface* chl-a and SST in the SAZ.

From the satellite spatial analysis, there was very little change in the day-to-day variability of chl-a at 66 km (mean range of standard deviation = 0.007). As there is very little change in spatial variability in time, it can be assumed through the power law relationship that the spatial variability of chl-a is dependent on the variability of physics at different scales. Therefore, according to the power law, the variance captured by the glider at this length scale should be similar to what the satellite captures. However, this is not the case as the glider is capturing more variability (mean standard deviation = 0.060) than the satellite (mean standard deviation = 0.019) (Figure 3.7). In their paper, Mahadevan and Campbell (2002) described a spatial growth term as the underlying theoretical reasons for this variability however in this study, the spatial growth term is not fully representative of what appears to be occurring in reality. A reason for this unexplained variability could be due to the SAZ having more small scale biological variability than the North Atlantic, which the glider is able to measure. Also, ocean colour satellite algorithms are known for underestimating chl-a concentrations, especially between (0.2-2 mg m^{-3}) in the Southern Ocean by 2-3 times (Dierssen and Smith 2000; Moore and Abbott 2000; Garcia et al. 2005; Mitchell and Kahru 2009; Kahru and Mitchell 2010). Therefore, the satellite could be failing to capture the greater variability measured by the glider.

Additionally, it cannot be said that there is a linear relationship between spatial and temporal variability that is causing phytoplankton variability but we can assume that the glider is measuring the growth term in time rather than in space. The reason for this conclusion is that if the growth term was from spatial variability, we would be able to observe it in the satellite images. Therefore, it can be concluded that one-third of the variability in phytoplankton measured by the glider is caused by spatial variability, while the remainder occurs from local adjustments in time (e.g. phytoplankton growth).

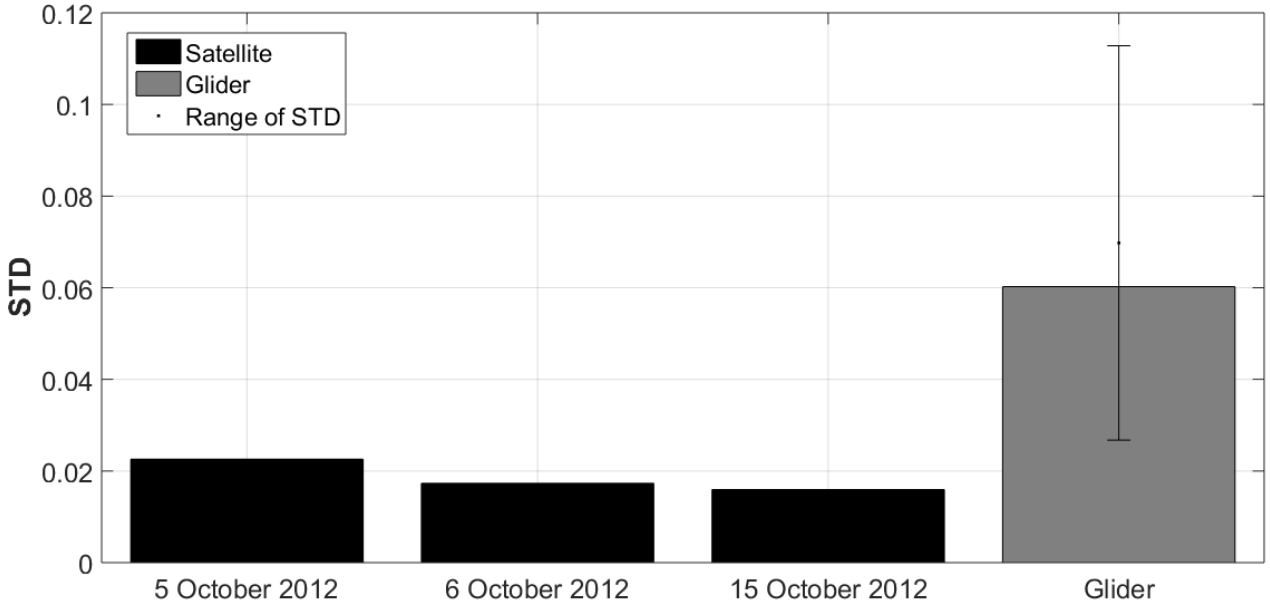

Figure 3.7 Spatial-temporal analysis of the standard deviation of satellite chl-a images (black) at 66 km and glider surface chl-a data (grey) in a 6 day period for spring.

3.5 Conclusion

Overall, the standard deviation for chl-a was higher at all length scales than SST. The comparison between the normalised slopes of the log-log *S(L)* curves showed that the power law exponents (measure of patchiness) of the SST (mean p = 0.59) were on average greater than those for chl-a (mean p = 0.40). This, implies that chl-a maintains a larger spatial variability than SST at small scales, indicating that chl-a is patchier than SST.

Initially, spatial analysis of the chl-a satellite images, indicated similar spatial variability of chl-a in spring (mean p = 0.33) and summer (mean p = 0.42), where phytoplankton is patchy across all length scales. Although there was very little difference in inter-seasonal patchiness of chl-a, there was an inter-seasonal difference in the standard deviation between spring and summer chl-a. This was thought to be primarily the result of increased growth rates in summer that allowed for higher maximum chl-a concentrations which in conjunction with submesoscale variability drove higher standard deviations. Additionally, on average there is a greater difference between spring chl-a and SST power law exponents (mean difference of p=0.2) than in summer which can be interpreted as larger patchiness in phytoplankton in spring compared to summer. This difference in seasonal patchiness, confirms what Swart et al. (2015) suggested in their study with gliders, that phytoplankton blooms in spring are patchy, whereas in summer the phytoplankton blooms appeared more homogenous in space.

Analysis of chl-a spatial variability from satellite data for consecutive days with surface chl-a from gliders helped us to determine that the glider was capturing almost triple the amount of surface chl-a variability than the satellite in spring. Additionally, it can be assumed that the glider is mainly measuring phytoplankton adjustments in time rather than in space as there was very little differences in spatial variance observed in the satellite images with time. Therefore, it is proposed that in the SAZ a third of the variability in phytoplankton measured by the glider is caused by spatial variability, while the remainder occurs from local adjustments in time.

Chapter 4:

Summary of results

4.1 An improved understanding of the spatial and temporal scales of variability in the Sub-Antarctic Zone

The Sub-Antarctic Zone (SAZ) is a region of the Southern Ocean were phytoplankton have high-annual and intra-seasonal variability (Thomalla et al., 2011). Increasing evidence has shown that seasonal to sub-seasonal temporal scales and meso- to submesoscales in the Southern Ocean play a prominent part in understanding the sensitivity of ocean primary productivity to climate change (Boyd, 2002; Fauchereau et al., 2011; Lévy et al., 2012; Swart et al., 2015). The varying spatial and temporal distribution of phytoplankton in the SAZ is due to the complex sub-seasonal nature of the interaction of light and nutrients through meso- and submesoscale features (Thomalla et al., 2011; Swart et al., 2015). Furthermore, the spatial and temporal distribution of phytoplankton differs inter-seasonally due to different dominant physical forcing mechanisms occurring during spring versus summer (Swart et al., 2015). Models (Levy et al., 2001; Glover et al., 2008) and observations (Arrigo et al., 2008; Thomalla et al., 2011; Swart et al., 2015) have shown the importance of understanding and resolving sub-seasonal and meso- to submesoscale variability of phytoplankton. This calls for a need to better understand the spatial and temporal variability of phytoplankton in order improve our understanding of the global carbon cycle.

A major problem in being able to understand or parametrise the meso- and submesoscale variability of phytoplankton and their drivers is the difficulty in adequately sampling at these scales. Spatial and seasonal variation of surface chlorophyll-a (chl-a) is currently most effectively monitored by satellites (Reilly et al., 1998; Marrari et al., 2006). Even though satellites provide high-resolution information on phytoplankton distribution, the high-resolution information is often removed by averaging of the data both in time and space due to large gaps in the data from clouds (Lévy et al., 2012). Gliders are able to determine high temporal and spatial resolution of chl-a and its corresponding variability (Eriksen et al., 2001). However, an issue that has been raised is about the quasi-Lagrangian nature of the gliders and the possibility that gliders sample the differences between meso- and submesoscale features rather than intrinsic changes within the water column.

This study used a 5.5 month data set obtained from an autonomous Seaglider that sampled at a high-resolution (average 1.4 km in space, 2.5 hours in time) during spring and summer in the SAZ. High-resolution (2 km) ocean colour satellite data from MODIS were also used to investigate the spatial variability of phytoplankton in the SAZ.

4.1.1 Temporal analysis

For the period of the glider deployment, the seasonal cycle was the overarching source of chl-a variability due to the SAZ being a light limited region. With the removal of the multi-seasonal signal, submesoscale variability dominated the surface chl-a time series. In both spring and summer, surface chl-a variability was dominated by similar submesoscale (~2, ~4 and ~9 day) signals that were driven by submesoscale variability in mixed layer depth (MLD) and wind stress. However, the drivers of variability differed inter-seasonally. In spring the submesoscale variability is likely caused by the weakening of the wind stress, which results in the restratification of the mixed layer through the slumping of the lateral density gradients from submesoscale eddies (Mahadevan et al., 2012; Swart et al., 2015) which in turn allows for instances of improved light environment that drives sporadic and patchy blooms. Whereas in summer, synoptic storm events that pass through the SAZ, vary the strength of the wind stress and introduce deepening and shoaling of the MLD at the meso- and submesoscale, which in turn causes both dilution and growth responses to improved nutrient supply from entrainment.

The temporal analysis showed that submesoscales drive the majority of the observed variability in surface chl-a. However, it is not always possible to sample at these scales, particularly in the Southern Ocean, and this work allowed us to determine a minimum sampling period. By subsampling at various frequencies the study was able to determine the minimum sampling period required to adequately capture sub-seasonal phytoplankton variability. Through reconstruction of the surface chl-a time series (mean and standard deviation), subsampling analysis found that sampling at periods of 10 days or less in both spring and summer is required to adequately resolve and characterise the seasonal scales of variability of phytoplankton in the SAZ.

4.1.2 Spatial analysis

Spatial analysis of the chl-a in the SAZ found phytoplankton to be patchier across all length scales compared to sea surface temperature (SST). This can be attributed to the longer response time of SST to heat flux than the time scales of biological uptake. Spatial analysis found that chl-a in summer is slightly less patchy than in spring, but that there is a higher variance in summer. Through the use of SST as a proxy for upper ocean physics, we know that spatial variability of physics is similar in spring and summer. The study proposes that in the SAZ, the persistence of physical processes in summer elevate nutrient concentrations, which together with sufficient summer light allows for greater growth to occur

in summer than in spring and is creating the observed offset in the chl-a variance between spring and summer.

Spatiotemporal analysis of satellite and glider data was used to address the quasi-Lagrangian nature of glider sampling. Analysis in spring found that the glider was capturing approximately triple the amount of surface chl-a variability than can be captured by the satellite using three subsequent images. Therefore, it is proposed that the variability observed in glider measurements in the SAZ is largely due to phytoplankton adjustments in time rather than by the glider sampling spatial submesoscale features with different surface chl-a concentrations.

4.2 Limitations and future work

Monitoring fine scale features of ocean processes has become important for understanding the role that the ocean plays in climate change. This study uses high-resolution glider and satellite data to sample sub-seasonal and meso- to submesoscale variability in surface chl-a. Despite this, there were some limitations in this study. I mention some of the limitations of this study and suggest improvements for future high-resolution studies on phytoplankton.

The SAZ is a region that has high phytoplankton inter-annual and intra-seasonal variability. In order to fully understand phytoplankton variability, spatial and temporal analysis needs to occur over a number of years. However, this study was limited to one seasonal study and only over the spring and summer A comparison of the EMD analysis from the second Seaglider deployed during the SOSCEx I experiment, would aid in determining the dominant modes of phytoplankton temporal variability during the spring and summer of 2012/2013. In SOSCEx II, a paired Seaglider and Wave Glider sampled in 'mooring mode' continuously for 4 months. Analysis of these 'mooring' gliders would assist in understanding phytoplankton temporal variability.

High-resolution (2 km) satellite data was used in order to observe daily spatial variability at small scales. This allowed for the identification of small scale variability but restricted the amount of days that had sufficient spatial coverage. Additionally, a direct day to day match of chl-a and SST satellite images was not possible. Therefore, the conclusions of this study are based on only the few days available throughout the period of this study. By analysing satellite data over a few years, a better understanding of phytoplankton spatial variability can be developed. Furthermore, a comparison of spatial variability in

regions throughout the SAZ and the Southern Ocean will improve our understanding of how the distribution of phytoplankton affects the carbon cycle.

References

Arhan, M., Speich, S., Messager, C., Dencausse, G., Fine, R. & Boye, M. 2011. Anticyclonic and cyclonic eddies of subtropical origin in the subantarctic zone south of Africa. *Journal of Geophysical Research*. 116(C11):C11004. DOI: 10.1029/2011JC007140.

Arrigo, K.R., Schnell, A., Lizotte, M.P. & Worthren, D. 1998. Primary production in Southern Ocean water. *Journal of Geophysical Research*. 103(C8):587–600.

Arrigo, K.R., van Dijken, G.L. & Bushinsky, S. 2008. Primary production in the Southern Ocean, 1997–2006. *Journal of Geophysical Research*. 113(C08004):1–27. DOI: doi:10.1029/2007JC004551.

Banse, K. 1994. Grazing and zooplankton production as key controls of phytoplankton production in the open ocean. *Oceanography*. 7:13–20.

Behrenfeld, M.J., Boss, E., Siegel, D.A. & Shea, D.M. 2005. Carbon-based ocean productivity and phytoplankton physiology from space. *Global Biogeochemical Cycles*. 19(1):1–14. DOI: 10.1029/2004GB002299.

Belkin, I.M. & Gordon, A.L. 1996. Southern Ocean fronts from the Greenwich meridian to Tasmania. *Journal of Geophysical Research*. 101(C2):3675. DOI: 10.1029/95JC02750.

Blain, S., Queguiner, B., Armand, L., Belviso, S., Bombled, B., Bopp, L., Bowie, A., Brunet, C., Brussaard, C., Carlotti, F., Christaki, U., Corbiere, A., Durand, I., Ebersbach, F., Fuda, J., Garcia, N., Gerringa, L., Griffiths, B., Guigue, C., Guillerm, C., Jacquet, S., Jeandel, C., Laan, P., Lefevre, D., Lo Monaco, C., Malits, A., Mosseri, J., Obernosterer, I., Park, Y., Picheral, M., Pondaven, P., Remenyi, T., Sandroni, V., Sarthou, G., Savoye, N., Scouarnec, L., Souhaut, M., Thuiller, D., Timmermans, K., Trull, T., Uitz, J., van Beek, P., Veldhuis, M., Vincent, D., Viollier, E., Vong, L. & Wagener, T. 2007. Effect of natural iron fertilization on carbon sequestration in the Southern Ocean. *Nature*. 446(7139):1070–1074. DOI: 10.1038/nature05700.

Boss, E. & Pegau, W.S. 2001. Relationship of light scattering at an angle in the backward direction to the backscattering coefficient. *Applied Optics*. 40(30):5503–5507.

Boyd, P.W. 2002. Environmental factors controlling phytoplankton processes in the Southern Ocean. *Journal of Phycology*. 38(5):844–861.

Boyd, P.W. & Ellwood, M.J. 2010. The biogeochemical cycle of iron in the ocean. *Nature Geoscience*. 3(10):675–682. DOI: 10.1038/ngeo964.

Boyd, P.W., Sherry, N.D., Berges, J.A., Bishop, J.K.B., Calvert, S.E., Charette, M.A., Giovannoni, S.J., Goldblatt, R., Harrison, P.J., Morgan S.B., Roy, S., Soon, M., Strom, S., Thibault, D., Vergin, K.L., Whitney, F.A. and Wong, C.S. 1999. Transformations of biogenic particulates from the pelagic to the deep ocean realm. *Deep Sea Research Part II: Topical Studies in Oceanography*. 46:2761–2792. DOI: 10.1016/S0967-0645(99)00083-1.

Boyd, P.W., Watson, A.J., Law, C.S., Abraham, E.R., Trull, T., Murdoch, R., Bakker, D.C., Bowie, A.R.,

Buesseler, K.O., Chang, H., Charette, M., Croot, P., Downing, K., Frew, R., Gall, M., Hadfield, M., Hall, J., Harvey, M., Jameson, G., LaRoche, J., Liddicoat, M., Ling, R., Maldonado, M.T., McKay, R.M., Nodder, S., Pickmere, S., Pridmore, R., Rintoul, S., Safi, K., Sutton, P., Strzepek, R., Tanneberger, K., Turner, S., Waite, A. & Zeldis, J. 2000. A mesoscale phytoplankton bloom in the polar Southern Ocean stimulated by iron fertilization. *Nature*. 407(6805):695–702.

de Boyer Montegut, C., Madec, G., Fischer, A.S., Lazar, A. & Iudicone, D. 2004. Mixed layer depth over the global ocean: An examination of profile data and a profile-based climatology. *Journal of Geophysical Research: Oceans*. 109(C12). DOI: 10.1029/2004JC002378.

Braun, A.J. 2008. Subtropical storms in the South Atlantic basin and their correlation with Australian east-coast cyclones.

Briggs, N., Perry, M.J., Cetinić, I., Lee, C., D'Asaro, E., Gray, A.M. & Rehm, E. 2011. High-resolution observations of aggregate flux during a sub-polar North Atlantic spring bloom. *Deep Sea Research Part I: Oceanographic Research Papers*. 58(10):1031–1039.

Buschmann, C. 1999. Photochemical and non-photochemical quenching coefficients of the chlorophyll fluorescence: comparison of variation and limits. *Photosynthetica*. 37(2):217–224.

Carranza, M.M. & Gille, S.T. 2015. Southern Ocean wind-driven entrainmetn enhances satellite chlorophyll-a through the summer. *Journal of Geophysical Research: Oceans*. 120:304–323. DOI: 10.1002/2014JC010203.Received.

Chisholm, S.W. 2000. Oceanography: stirring times in the Southern Ocean. *Nature*. 407(6805):685–687.

Crumpton, W.G. & Wetzel, R.G. 1982. Effects of Differential Growth and Mortality in the Seasonal Succession of Phytoplankton Populations in Lawrence Lake, Michigan. *Ecology*. 63(6):1729–1739.

Cunningham, S.A., Alderson, S.G. & King, B.A. 2003. Transport and variability of the Antarctic Circumpolar Current in Drake Passage. *Journal of Geophysical Research*. 108(C5):8084. DOI: 10.1029/2001JC001147.

Deacon, G.E. 1933. A general account of the hydrology of the South Altantic Ocean. *Discovery*. 7:177–238.

Dickey, T.D. & Perry, M.J. 2008. Introduction to the Limnology and Oceanography Special Issue on Autonomous and Lagrangian Platforms and Sensors (ALPS). 53:2057–2061.

Dierssen, H. & Smith, R.. 2000. Bio-optical properties and remote sensing ocean color algorithms for Antarctic Peninsula waters. *Journal of Geophysical Research*. 105(C11):301–312.

du Plessis, M.D. 2014. Dynamics and variability of the Subantarctic mixed-layer as determined from a high-resolution glider dataset. University of Cape Town.

Eriksen, C.C. & Perry, M.J. 2009. The nurturing of seagliders by the National Oceanographic Partnership Program. *Oceanography*. 22(2):146.

Eriksen, C.C., Osse, T.J., Light, R.D., Wen, T., Lehman, T.W., Sabin, P.L., Ballard, J.W. & Chiodi, A.M. 2001. Seaglider : A Long-Range Autonomous Underwater Vehicle for Oceanographic Research. *The Journal of Oceanic Engineering*. 26(4):424–436.

Fauchereau, N., Tagliabue, A., Bopp, L. & Monteiro, P.M.S. 2011. The response of phytoplankton biomass to transient mixing events in the Southern Ocean. *Geophysical Research Letters*. 38(L17601). DOI: 10.1029/2011GL048498.

Fernand, L., Weston, K., Morris, T., Greenwood, N., Brown, J. & Jickells, T. 2013. The contribution of the deep chlorophyll maximum to primary production in a seasonally stratified shelf sea, the North Sea. *Biogeochemistry*. 113(1-3):153–166.

Frajka-Williams, E., Rhines, P.B. & Eriksen, C.C. 2009. Physical controls and mesoscale variability in the Labrador Sea spring phytoplankton bloom observed by Seaglider. *Deep Sea Research Part I: Oceanographic Research Papers*. 56(12):2144–2161. DOI: 10.1016/j.dsr.2009.07.008.

Franz, B.A., Bailey, S.W., Eplee, R.E., Feldman, G.C., Kwiatkowska, E., Mcclain, C., Meister, G., Patt, F.S., Thomas, D. & Werdell, R.J. 2005. The continuity of ocean color measurements from SeaWiFS to MODIS. In *Optics & Photonics 2005. International Society for Optica and Photonics*. 58820W–58820W.

Garcia, C.A.E., Garcia, V.M.T. & McClain, C.R. 2005. Evaluation of SeaWiFS chlorophyll algorithms in the Southwestern Atlantic and Southern Oceans. *Remote Sensing of Environment*. 95(1):125–137.

Gille, S.T. 2002. Warming of the Southern Ocean Since the 1950s. *Science*. 295(5558):1275–1277. DOI: 10.1126/science.1065863.

Glover, D.M., Doneym, S.C., Nelsonm, N.B. & Wallis, A. 2008. Submesoscale anisotropy (fronts, eddies, and filaments) as observed near Bermuda with ocean color data. In *Ocean Science Meeting*. 02–07.

Goebel, N.L., Frolov, S. & Edwards, C.A. 2014. Complementary use of Wave Glider and satellite measurements: Description of spatial decorrelation scales in Chl-a fluorescence across the Pacific basin. *Methods in Oceanography*. 10:90–103. DOI: 10.1016/j.mio.2014.07.001.

Gould, W.J., Roemmich, D., Wijffels, S., Freeland, H., Ignaszewsky, M., Jianping, X., Pouliquen, S., Desaubies, Y., Send, U., Radhakrishnan, K. & Takeuchi, K. Argo profiling floats bring new era of in situ ocean observations Argo Profiling Floats Bring New Era of In Situ Ocean Observations. *Eos*. 85(19):179–184. DOI: 10.1029/2004EO190002.

Gruber, N., Gloor, M., Fletcher, S.E.M., Doney, S.C., Dutkiewicz, S., Follows, M.J., Gerber, M., Jacobson, A.R., Joos, F., Lindsay, K., Menemenlis, D., Mouchet, A., Muller, S.A. Sarmiento, J.L. &Takahashi, T. 2009. Oceanic sources, sinks, and transport of atmospheric CO2. *Global Biogeochemical Cycles*. 23(1):1–21. DOI: 10.1029/2008GB003349.

Huang, N.E., Shen, Z., Long, S.R., Wu, M.C., Shih, H.H., Zheng, Q., Yen, N., Tung, C.C. & Liu, H.H. 1998. The empirical mode decomposition and the Hilbert spectrum for nonlinear and non-stationary time series analysis. *Proceedings: Mathematical, Physical and Engineering Sciences*. 454(1971):903–995. Available: http://www.jstor.org/stable/53161.

Ito, T. & Follows, M.J. 2003. Upper ocean control on the solubility pump of CO₂. *Journal of Marine Research*. 61(4):465–489. DOI: 10.1357/002224003322384898.

Joubert, W.R., Swart, S., Tagliabue, A., Thomalla, S.J. & Monteiro, P.M.S. 2014. The sensitivity of primary productivity to intra-seasonal mixed layer variability in the sub-Antarctic Zone of the Atlantic Ocean. *Biogeosciences Discussions*. 11(3):4335–4358. DOI: 10.5194/bgd-11-4335-2014.

Kahru, M. & Mitchell, B.G. 2010. Blending of ocean colour algorithms applied to the Southern Ocean. *Remote Sensing Letters*. 1(2):119–124.

Kaufman, D.E., Friedrichs, M.A.M., Smith, W.O., Queste, B.Y., Heywood, K.J. & Sea, R. 2014. Deep-Sea Research I Biogeochemical variability in the southern Ross Sea as observed by a glider deployment. *Deep Sea Research Part I: Oceanographic Research Papers*. 92:93–106.

Klein, P. & Lapeyre, G. 2009. The Oceanic Vertical Pump Induced by Mesoscale and Submesoscale Turbulence. *Annual Review of Marine Science*. 1:351–375. DOI: 10.1146/annurev.marine.010908.163704.

Large, W.G. & Pond, S. 1981. Open Ocean Momentum Flux Measurements in Moderate to Strong Winds. *Journal of Physical Oceanography*. 11(3):324–336.

Levitus, S., Conkright, M., Reid, J., Najjar, R. & Mantyla, A. 1993. Distribution of nitrate, phosphate and silicate in the world ocean. *Progress in Oceanography*. 31:245–273.

Levy, M., Klein, P. & Treguier, A.M. 2001. Impact of sub-mesoscale physics on production and subduction of phytoplankton in an oligotrophic regime. *Journal of Marine Research*. 59(4):535–565.

Levy, M., Jahn, O., Dutkiewicz, S. & Follows, M.J. 2014. Phytoplankton diversity and community structure affected by oceanic dispersal and mesoscale turbulence. *Limnology and Oceanography:Fluids and Environments*. 4(Pulliam 1988):67–84. DOI: 10.1215/21573689-2768549.

Lévy, M., Iovino, D., Resplandy, L., Klein, P., Madec, G., Tréguier, a.-M., Masson, S. & Takahashi, K. 2012. Large-scale impacts of submesoscale dynamics on phytoplankton: Local and remote effects. *Ocean Modelling*. 43-44:77–93. DOI: 10.1016/j.ocemod.2011.12.003.

Lévy, M., Ferrari, R., Franks, P.J.S., Martin, A.P. & Rivière, P. 2012. Bringing physics to life at the submesoscale. *Geophysical Research Letters*. 39(L14602). DOI: 10.1029/2012GL052756.

Mahadevan, A. 2016. The Impact of Submesoscale Physics on Primary Productivity of Plankton. *Annual review of marine science*. 8:161–84. DOI: 10.1146/annurev-marine-010814-015912.

Mahadevan, A. & Archer, D. 2000. Modeling the impact of fronts and mesoscale circulation on the nutrient supple and biogeochemistry of the upper ocean. *Journal of Geophysical Research*. 105(C1):1209–1225.

Mahadevan, A. & Campbell, J.W. 2002. Biogeochemical patchiness at the sea surface. *Geophysical Research Letters*. 29(19):1926. DOI: 10.1029/2001GL014116.

Mahadevan, A., D'Asaro, E., Lee, C. & Perry, M.J. 2012. Eddy-driven stratification initiates North Atlantic spring phytoplankton blooms. *Science*. 337:54–58. DOI: 10.1126/science.1218740.

Marrari, M., Hu, C. & Daly, K. 2006. Validation of SeaWiFS chlorophyll a concentrations in the Southern Ocean: A revisit. *Remote Sensing of Environment*. 105(4):367–375.

Martin, A.P. 2003. Phytoplankton patchiness: the role of lateral stirring and mixing. *Progress in Oceanography*. 57(2):125–174. DOI: 10.1016/S0079-6611(03)00085-5.

Martin, A.P., Richards, K.J., Bracco, A. & Provenzale, A. 2002. Patchy productivity in the open ocean. *Global Biogeochemical Cycles*. 16(2):1–9.

McGillicuddy Jr., D.J. 2016. Mechanisms of Physical-Biological-Biogeochemical Interaction at the Oceanic Mesoscale. *Marine Science*. 8. DOI: 10.1146/annurev-marine-010814-015606.

McGillicuddy Jr., D.J., Robinson, A., Siegel, D.A., Jannasch, H., Johnson, R., Dickey, T., McNeil, J., Michaels, A. & Knap, A.H. 1998. Influence of mesosclae eddies on new production in the Sargasso Sea. *Nature*. 394(6690):263–266.

McNeil, B.I., Tilbrook, B. & Matear, R.J. 2001. Accumulation and uptake of anthropogenic CO2 in the Southern Ocean, south of Australia between 1968 and 1996. *Journal of Geophysical Research: Oceans*. 106(C12):31431–31445.

McNeil, B.I., Metzl, N., Key, R.M., Matear, R.J. & Corbiere, A. 2007. An empirical estimate of the Southern Ocean air-sea CO2 flux. *Global Biogeochemical Cycles*. 21(3):1–16. DOI: 10.1029/2007GB002991.

Metzl, N., Tilbrook, B. & Poisson, A. 1999. The annual f CO2 cycle and the air – sea CO2 flux in the sub-Antarctic Ocean. *Tellus B*. 51(4):849–861.

Mikaloff Fletcher, S.E., Gruber, N., Jacobson, A.R., Doney, S.C., Dutkiewicz, S., Gerber, M., Follows, M., Joos, F., Lindsay, K., Menemenlis, D., Mouchet, A., Muller, S.A. & Sarmiento, J.L.. 2006. Inverse estimates of anthropogenic CO 2 uptake, transport, and storage by the ocean. *Global Biogeochemical Cycles*. 20:GB2002.

Mitchell, B.G. & Kahru, M. 2009. Bio-Optical Algorithms for ADEOS, GLI. *Journal of the Remote Sensing Society of Japan*. 29(1):80–85.

Monteiro, P.M.S., Boyd, P. & Bellerby, R. 2011. Role of the seasonal cycle in coupling climate and carbon cycling in the Subantarctic Zone. *Eos, Transactions American Geophysical Union*. 92(28):235. DOI: 10.1029/2011EO280007.

Moore, J. & Abbott, R. 2000. Phytoplankton chlorophyll distributions and primary production in the Southern Ocean. *Journal of Geophysical Research*. 105(C12):709–722.

Moore, J.K. & Abbott, M.R. 2002. Surface chlorophyll concentrations in relation to the Antarctic Polar Front : seasonal and spatial patterns from satellite observations. *Journal of Marine Research*. 37:69–86.

Nicholson, S. 2016. Intra-Seasonal Variability of Southern Ocean Primary Production : the Role of Storms and Mesoscale Intra-Seasonal Variability of Southern Ocean Primary Production : the Role of Storms and Mesoscale Turbulence. UPMC-Universite Paris 6 Pierre et Marie Curie; University of Cape Town.

Niewiadomska, K., Claustre, H., Prieur, L. & D'Ortenzio, F. 2008. Submesoscale physical-biogeochemical coupling across the Ligurian Current (northwestern Mediterranean) using a bio-optical glider. *Limnology and Oceanography*. 53(5):2210–2225.

Olbers, D., Borowski, D., Völker, C. & Wolff, J.O. 2004. The dynamical balance, transport and circulation of the Antarctic Circumpolar Current. *Antarctic Science*. 16(4):439–470. DOI: 10.1017/S0954102004002251.

Orsi, H., Whitworth, T. & Worth, D.N. 1995. On the meridional extent and fronts of the Antarctic Circumpolar Current. *Deep Sea Research Part I: Oceanographic Research Papers*. 42(5):641–673.

Pasquero, C., Bracco, A. & Provenzale, A. 2005. Impact of the spatiotemporal variability of the nutrient flux on primary productivity in the ocean. *Journal of Geophysical Research*. 110:C07005. DOI: 10.1029/2004JC002738.

Perry, M.J., Sackmann, B., Ekriksen, C.. & Lee, C.M. 2008. Seaglider observations of blooms and subsurface chlorophyll maxima off the Washington coast. *Limnology and Oceanography*. 53(5):2169–2179.

Pinot, J. M., Tintori, J. & Gomis, D. 1995. Pergamon Multivariate analysis of the surface circulation in the Balearic Sea. *Progress in Oceanography*. 36(4):343–376.

Pollard, R.T., Salter, I., Sanders, R.J., Lucas, M.I., Moore, C.M., Mills, R.A., Statham, P.J., Allen, J.T., Baker, A.R., Bakker, D.C.E., Charette, M.A., Fielding, S., Fones, G.R.,French, M., Hickman, A.E., Holland, R.J., Hughes, J.A., Jickells, T.D., Lampitt, R.S., Morris, P.J., Nedelec, F.H., Nielsdottir, M., Planquette, H., Popova, E.E., Poulton, A.J., Read, J.F., Seeyave, S., Smith, T., Stinchcombe, M., Taylor, S., Thomalla, S., Venalbes, H.J., Williamson, R. & Zubkov, M.V. 2009. Southern Ocean deep-water carbon export enhanced by natural iron fertilization. *Nature*. 457(7229):577–580. DOI: 10.1038/nature07716.

Queste, B.Y., Heywood, K.J., Kaiser, J., Lee, G.A., Matthews, A., Schmidtko, S., Walker-brown, C. & Woodward, S.W. 2012. *Deployments in extreme conditions : Pushing the boundaries of Seaglider capabilities*.

Rato, R.T., Ortigueira, M.D. & Batista, A. G. 2008. On the HHT, its problems, and some solutions. *Mechanical Systems and Signal Processing*. 22(6):1374–1394. DOI: 10.1016/j.ymssp.2007.11.028.

Reilly, J.E.O., Maritorena, S., Mitchell, B.G., Siegel, D.A., Carder, K.L., Garver, S.A., Kahru, M. & Mcclain, C. 1998. Ocean color chlorophyll algorithms for SeaWiFS. *Journal of Geophysical Research*. 103(Cll):937–953.

Rodgers, K.B., Sarmiento, J.L., Aumont, O., Crevoisier, C., de Boyer Monte, C. & Metzl, N. 2008. A wintertime uptake window for anthropogenic CO2 in the North Pacific. *Global Biogeochemical Cycles*. 22(2):1–16. DOI: 10.1029/2006GB002920.

Roemmich, D., Riser, S., Davis, R.E. & Desaubies, Y. 2004. Autonomous Profiling Floats : Workhorse for Broad-scale Ocean Observations. *Marine Technology Society Journal*. 38(1):31–39.

Rudnick, D.L., Davis, R.E., Eriksen, C.C., Fratantoni, D.M. & Perry, M.J. 2004. Underwater Gliders for Ocean Research. *Marine Technology Society Journal*. 38(2):48–59.

Sackmann, B.S., Perry, M.J. & Eriksen, C.C. 2008. Seaglider observations of variability in daytime fluorescence quenching of chlorophyll- a in Northeastern Pacific coastal waters. *Biogeosciences Discussions*. 5:2839–2865.

Salle, J.B., Llort, J., Tagliabue, A. & Levy, M. 2015. Characterization of distinct bloom phenology regimes in the Southern Ocean. *ICES Jounral of Marine Science: Journal du Conseil*. fsv069.

Schlitzer, R. 2002. Carbon export fluxes in the Southern Ocean: results from inverse modeling and comparison with satellite-based estimates. *Deep Sea Research Part II: Topical Studies in Oceanography*. 49:1623–1644. DOI: 10.1016/S0967-0645(02)00004-8.

Senam, T. 2015. An investigation into the sampling bias of Argo profiling floats in the Southern Ocean. Univeristy of Cape Town.

Sokolov, S. & Rintoul, S.R. 2007. Multiple Jets of the Antarctic Circumpolar Current South of Australia*. *Journal of Physical Oceanography*. 37(5):1394–1412.

Spall, S.A. & Richards, K.J. 2000. A numerical model of mesoscale frontal instabilities and plankton dynamics - I . Model formulation and initial experiments. *Deep Sea Research Part I: Oceanographic Research Papers*. 47(7):1261–1301.

Stramski, D., Reynolds, R.A., Kahru, M. & Mitchell, B.G. 1999. Estimation of Particulate Organic Carbon in the Ocean from Satellite Remote Sensing. *Science*. 285(5425):239–242.

Sverdrup, H.U. 1953. On Conditions for the Vernal Blooming of Phytoplankton. *Journal du Conseil*. 18(3):287–295.

Swart, S. & Speich, S. 2010. An altimetry-based gravest empirical mode south of Africa: 2. Dynamic nature of the Antarctic Circumpolar Current fronts. *Journal of Geophysical Research*. 115(C03003). DOI: 10.1029/2009JC005300.

Swart, S., Chang, N., Fauchereau, N., Joubert, W., Lucas, M., Mtshali, T., Roychoudhury, A., Tagliabue, A., Thomalla, S., Waldron, H. & Monteiro, .P.M.S. 2012. Southern Ocean Seasonal Cycle Experiment 2012: Seasonal scale climate and carbon cycle links. *South African Journal of Science*. 108(3/4):3–5.

Swart, S., Thomalla, S.J. & Monteiro, P.M.S. 2015. The seasonal cycle of mixed layer dynamics and phytoplankton biomass in the Sub-Antarctic Zone : A high-resolution glider experiment. *Journal of Marine Systems*. 147:103–115. DOI: 10.1016/j.jmarsys.2014.06.002.

Takahashi, T., Sweeney, C., Hales, B., Chipman, D.W., Newberger, T., Goddard, J.G., Iannuzzi, R.A. & Sutherland, S.C. 2012. The changing carbon cycle in the Southern Ocean. *Oceanography*. 25(3):26–37.

Thomalla, S., Gilbert, O.A., Vichi, M. & Swart, S. 2016. Using optical sensors in gliders to estimate phytoplankton carbon concentrations and chlorophyll-to-carbon ratios in the Southern Ocean.

Thomalla, S.J., Fauchereau, N., Swart, S. & Monteiro, P.M.S. 2011. Regional scale characteristics of the seasonal cycle of chlorophyll in the Southern Ocean. *Biogeosciences*. 8(10):2849–2866. DOI: 10.5194/bg-8-2849-2011.

Trull, T.W., Bray, S.G., Manganini, S.J., Honjo, S. & Francois, R. 2001. Moored sediment trap measurements of carbon export in the Subantarctic and Polar Frontal Zones of the Southern Ocean, south of Australia. *Journal of Geophysical Research: Oceans*. 106(C12):31489–31509.

Van Gennip, S., Martin, A.P., Srokosz, M.A., Allen, J.T., Pidcock, R., Painter, S.C. & Stinchcombe, M.C. 2016. Plankton patchiness investigated using simultaneous nitrate and chlorophyll. *Journel of Geophysical Research: Oceans*. DOI: 10.1002/2016JC011789.

Wang, X., Matear, R.J. & Trull, T.W. 2001. Special Section: The SAZ Project-Modeling seasonal phosphate exported and resupply in the Subantarctic and Polar Frontal Zones in the Australian sector of the Southern Ocean (Paper 2000JC000645). *Journal of Geophyiscal Research-Part C-Oceans*. 106(12):31525–31542.

Xing, X., Claustre, H., Blain, S., D'Ortenzio, F., Antoine, D., Ras, J. & Guinet, C. 2012. Quenching correction for in vivo chlorophyll fluorescence acquired by autonomous platforms : A case study with instrumented elephant seals in the Kerguelen region (Southern Ocean). *Limnnology and Oceanography*. 10:483–495. DOI: 10.4319/lom.2012.10.483.

Zhang, X. & Hu, L. 2009. Scattering by pure seawater at high salinity. *Optics Express*. 17(15):12685–12691.

Zhang, H.-M., Bates, J.J. & Reynolds, R.W. 2006. Assessment of composite global sampling: Sea surface wind speed. *Geophysical Research Letters*. 33(17):L17714. DOI: 10.1029/2006GL027086.

Zhang, X., Hu, L. & He, M.-X. 2009. Scattering by pure seawater : Effect of salinity. *Optics Express*. 17(7):5698–5710.